An Abstract of the Thesis of

David J. Yarger for the degree of Master of Science in Mechanical Engineering presented on August 23, 2007.

Title: Design Considerations for a Miniature Atmospheric Engine with a Magnet-Actuated Autonomously-Reciprocating In-Cylinder Regenerator for Portable Power Production.

Abstract approved:

Richard B. Peterson

Driven by the need for high energy-density power sources, demand has stimulated the development of small-scale engines. A small-scale engine with a fuel supply could replace batteries and utilize higher energy-density liquid hydrocarbon fuels; such an advance could deliver a new age of portable devices. Currently, operable small-scale engines exist; yet their efficiencies are poor. One possible alternative for improving efficiency is the incorporation of thermal regeneration. This thesis develops a concept for an efficient miniature reciprocating engine for portable power production that is based upon the regenerated atmospheric cycle and uses a magnet-actuated in-cylinder regenerator. As part of the development of the proposed engine, a dynamic model of the regenerator was developed concurrently with an engine simulator. The dynamic model was validated using the engine simulator and can now be used to develop a model to

study the thermal aspects of regeneration. The engine simulator was also used to study a unique lubrication-free low-friction piston-cylinder set that utilizes a graphite-glass clearance seal. The piston cylinder set was subjected to several pressure tests, including one with a 26 h duration. It was found that with the addition of aspiration slots, the piston cylinder set with the engine simulator operating at 1800 rpm could reach a peak pressure of approximately 370 kPa with a pressure ratio of approximately 4.2. For the 26 h long-duration test, it was found that the graphite piston did not show any significant wear. However, elastomer cups that were part the ball-joint supports for the piston did exhibit wear that lead to a decrease in peak cycle pressure with time.

Design Considerations for a Miniature Atmospheric Engine with a Magnet-Actuated Autonomously-Reciprocating In-Cylinder Regenerator for Portable Power Production

by
David J. Yarger

A Thesis

submitted to

Oregon State University

in partial fulfillment of
the requirements for the
degree of

Master of Science

Presented August 23, 2007
Commencement June 2008

Master of Science thesis of David J. Yarger presented on August 23, 2007.

APPROVED:

Major Professor, representing Mechanical Engineering

Head of the Department of Mechanical Engineering

Dean of the Graduate School

I understand that my thesis will become part of the permanent collection of Oregon State University libraries. My signature below authorizes release of my thesis to any reader upon request.

David J. Yarger, Author

Acknowledgements

I would like to acknowledge several professors who have contributed to my education at Oregon State University. Dr. Richard Peterson has been a wonderful mentor throughout the years; and his industry has supported this research, which has been integral to my education. His is a gift I will carry through life. Dr. John Lee taught me how to properly write mathematics; during this process, my thinking about the subject became clearer. Dr. Brian Bay emphasized that the purpose of an experiment should be known before performing an uncertainty analysis. Dr. Vicki Tolar Burton let me know that it is alright to occasionally split an infinitive.

Also, many friends have assisted with this work. Cary Maunder was always available for support and MATLAB help. Scott Chewning readily offered his assistance and pragmatic advice. Tom Herron, with whom I've enjoyed many thoughtful conversations, was always available for his insight. Sara Gallops kindly lent me her camera.

To all of those mentioned here, I express sincere gratitude.

Many journeys end here; but, the secret's told the same. Life is just a candle, and a dream must give it flame.

—Rush, "The Fountain of Lamneth"

Table of Contents

Table of Contents (Continued)

List of Appendices

List of Figures

List of Figures (Continued)

List of Tables

List of Nomenclature

A	surface area of regenerator normal to flow
c	width of yoke
C_P	coefficient for force from pressure difference across regenerator
C_V	coefficient for drag force
d	regenerator diameter
F_{Bottom}	normal force present in bottom dwell phase
$F_{Coupled}$	normal force present in coupled phase
F_M	magnetic attraction force
F_P	force from pressure difference across regenerator
F_S	return spring force
F_{Top}	normal force present in top dwell phase
F_V	drag force
$F_{V,Gap}$	drag force from clearance gap
$F_{V,Ports}$	drag force from regenerator ports
g	local acceleration from gravity
h_{Mag}	magnet pole offset
h_{Min}	yoke minimum height
H	regenerator height
k	ratio of specific heats, C_p/C_v
k_{Mag}	magnetic attraction force constant
l	length of connecting rod
m	mass of regenerator
n	number of regenerator ports
p	regenerator port diameter
P	pressure
P_{Atm}	atmospheric pressure
P_{Max}	maximum pressure
P_{Min}	minimum pressure
P_R	pressure ratio
P_{RAtm}	pressure ratio with respect to atmospheric pressure
r	expansion ratio, V_1/V_3, or radius of drive rotor
S_*	standard deviation for measurement $*$
$t_{i,*}$	student-t statistic for i degrees of freedom and a confidence of $*$ %
T_*	temperature at state $*$
u_*	uncertainty for component $*$
U_*	overall uncertainty for measurement $*$
V	volume

List of Nomenclature (Continued)

V_*	output voltage for condition $*$
x_P	position of piston
x_R	position of regenerator
w	width of clearance gap or pitch diameter of drive gear
α	velocity amplification factor
ϵ	regenerator effectiveness
η	thermal efficiency
θ	rotor angle
μ	dynamic viscosity of air
τ	temperature ratio, T_1/T_2

This work is dedicated to my mother, who has
always believed in my scholarship. And, to
my father, who has been the symbol of
integrity for my family.

Deeply I love you both.

1 Introduction

Development of small-scale engines is driven by the demand for high energy-density power sources. The fabrication of small-scale devices, alone, is challenging. In addition to this usual challenge, small-scale engine development is further complicated by heat transfer effects and frictional effects. This chapter provides a context for small-scale engine development, presents the idea of regeneration, and discusses the scope of this thesis. Researchers are developing several types of small-scale engines. Many of these engines are based upon familiar designs (e.g. Wankel engines, turbine engines, and reciprocating engines). However, some of them are unlike any large-scale engine and have the specific purpose of generating electrical power. The use of regenerative heat transfer in internal combustion engines has the potential to significantly increase efficiency, yet regeneration has not been applied to small-scale engines. This thesis develops a concept for an efficient miniature reciprocating engine for portable power production that, unlike any other known concept with similar requirements, incorporates regenerative heat exchange.

1.1 Development of Small-Scale Engines

Driven by the need for high energy-density power sources, demand has stimulated the development of small-scale engines. A small-scale engine with a fuel supply could replace batteries, having an energy density of about 1.2 kJ/g, and utilize the higher energy density of liquid hydrocarbon fuels, which is about 42 kJ/g [1]. Currently, the efficiency of small-scale engines is so poor that batteries still provide the greatest energy density for small-scale power applications. But, the development of a small-scale engine with a minimal balance-of-plant and an efficiency of just 15 % could deliver a new age of portable devices.

Small-scale engines pose obstacles caused by their size. For larger engines, temperature isolation, which is necessary for successful and efficient operation, can be maintained due to amenable separation distances between the hot and cold regions of the engine. However when these distances are smaller, temperature isolation becomes intractable because of high temperature gradients, which lead to high heat transfer rates [2]. In addition to this difficulty, frictional effects are amplified on this small scale, where the size of the friction surfaces is relatively large; frictional effects alone can stifle the development of a particular small-scale engine concept. Both of these challenges must be addressed while designing a small-scale engine: a shift from the traditional view of a prime mover is required.

Research is underway on small-scale engines to produce power for the following applications:

- unmanned air vehicles [3–5];
- unmanned ground vehicles [6];
- wearable devices for commercial and military applications [7];
- portable electronics (e.g. laptops and wireless communication devices);
- portable lighting and household appliances [8];
- multifunction devices (e.g. a device that could serve as a generator, heater, and stove) [6];

- artificial organs [9];
- and exoskeleton systems [9].

Some of the engines proposed are small versions of familiar designs. For example, researchers are exploring small-scale embodiments of Wankel engines, turbine engines, and reciprocating engines. On the other hand, several novel engines are in development that would utilize mechanisms designed solely for electrical power output. Many small-scale engine research efforts are discussed below; and to clarify relative scale and application, Table 1.1 quantitatively relates power to both an abiotic example and a biotic example [9].

Researchers are developing several types of rotary engines for small-scale power production. The Wankel engine design is thought of as a good candidate for miniaturization because of its simple rotary motion and lack of valves. Fernandez-Pello et al., from the University of California, Berkeley, have been developing a micro-Wankel engine [8]. Fernandez-Pello believes, if successful, it could be used for electronic devices, portable lighting, and household appliances. A working penny-sized prototype, with a theoretical output of 3 W to 40 W depending on engine speed, has been constructed using electrical-discharge machining. The prototype is a step toward creating a device about the size of a square millimeter. Researchers at the University of Birmingham

Table 1.1: Power related to an abiotic example and a biotic example [9].

Power, W	Abiotic Example	Biotic Example
1000	Microwave Oven	Horse
100	Light Bulb	Human
10	Small Laptop	Bat
1	Mobile Phone	Hummingbird
0.01	Pager	Fly

are also developing a small-scale Wankel engine [10]. Their design, which has a theoretical output of 12 W at 17,000 rpm, is focused on two-dimensional geometry so the engine can be fabricated using an advanced ultraviolet-lithography process.

Several small-scale turbine engines are also in development. At the Massachusetts Institute of Technology, Epstein et al. are developing a shirt-button sized micro-turbine engine to either produce electrical power for electronics or thrust for unmanned vehicles [5, 12]. Figure 1.1 is a drawing from Epstein's 1999 patent showing a cross section of the micro-turbine engine, which has a rotor diameter of 4 mm [11]. The multipurpose engine has theoretical outputs of either 10 W of electrical power or 0.1 N of thrust depending upon the application. Engine prototypes are being created out of etched silicon parts, which are made using processes similar to those required for computer chips. Epstein claims the main challenge is heat management. Larger turbine engines, with theoretical outputs of 28 W, 50 W, and 100 W, are also in development at the Catholic University of Leuven, the Jet Propulsion Laboratory, and the Ishikawajima-Harima Heavy Industries Company of Japan, respectively [13–15].

Researchers are also considering reciprocating engines for small-scale power applications. D-STAR Engineering is developing a multifunction device, known as a miniature generator set, from a reciprocating engine that uses a two-stroke Diesel cycle with a theoretical output of 80 W [6]. The device, which has an overall size of 13 cm × 13 cm, is designed to be used as a generator, heater, and stove for tactical

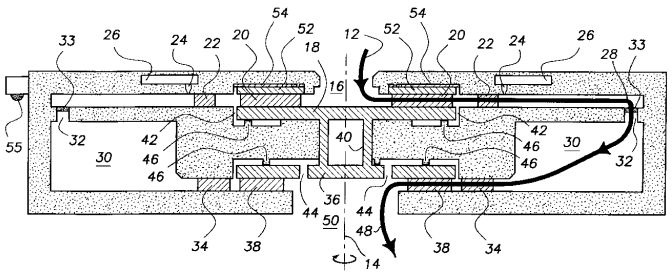

Figure 1.1: A drawing from Epstein's 2002 patent showing a cross section of the proposed micro-turbine engine [11].

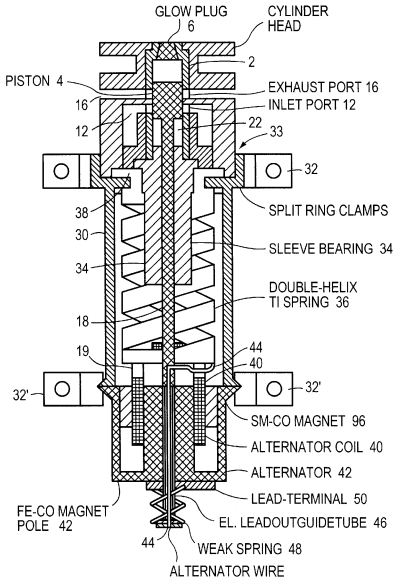

Figure 1.2: A drawing from Annen's 2002 patent showing the miniature internal combustion engine (MICE) that was designed to produce electrical power [16].

purposes. It has been tested and can provide 50 W of electrical power for a period 36 h.

For many portable power applications, electrical power is the sole requirement; several novel engines are in development for this purpose only. Annen et al. are developing a miniature internal combustion engine (MICE) that produces only electrical power [3, 4]. Figure 1.2 shows a drawing of the MICE from Annen's 2002 patent [16]. The piston is coupled to a linear electric generator and a spring, and the engine is intended to operate at the resonant frequency of the mass-spring system. Because all of the motion is linear, the MICE has little friction and was designed for lubrication-free operation. Versions designed for 10 W and 500 W applications have been constructed and demonstrated. The 10 W prototype excluding a fuel supply is approximately the size of an AA battery (50 mm in length with a diameter of 14 mm). At the University of Michigan, Dahm et al. are developing a micro internal combustion swing engine (MICSE) for applications requiring 20 W that generates electrical power from a rotationally oscillating motion [7]. The researchers consider the swing engine a good

candidate for miniaturization because of its simple motion and lack of a need for a starting system.

At Pennsylvania State University, a research effort is underway to design a solid piston micro-engine [17]. The proposed engine would use the thermal expansion and contraction of a solid piston to actuate a piezoelectric transducer to convert mechanical energy into electrical energy. Experiments on a cyclically pulsed catalytic micro-combustor running on hydrogen fuel have been completed as a step toward a successful design.

1.2 Regeneration in Combustion Engines

The Stirling engine was invented in 1816, and perhaps the most significant feature of the invention was to economize the thermodynamic cycle by using an internal heat exchanger known as a regenerator [18]. But, a regenerator is not simply a heat exchanger: it also functions as a thermal-energy storage device. In a reciprocating engine, where the fluid flow through the regenerator is also reciprocating, the regenerator takes thermal energy from one process of the cycle and delivers it to another. Turbine engines, which utilize thermodynamic processes separated in space, can use a subtly different component called a recuperator, which is a counterflow heat exchanger that transfers heat from the exhaust to the working fluid before combustion [19]. Unlike a recuperator, a regenerator is not a steady state heat exchanger. It must transfer heat between thermodynamic processes separated in time: this is a detail that severely complicates both the modeling of thermal regeneration and the design of a regenerator.

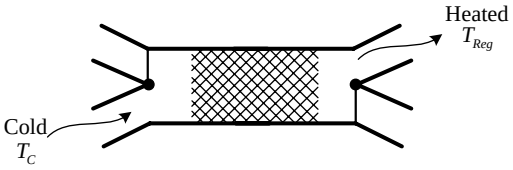

(a) The heating blow of the regenerator.

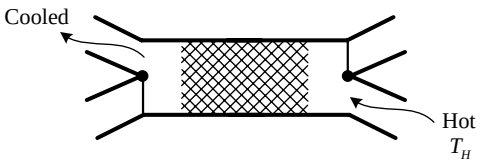

(b) The cooling blow of the regenerator.

Figure 1.3: Blows of the idealized regeneration process.

The idealized regeneration process, shown in Fig. 1.3, can be thought of as a cyclical series of working-fluid movements, known as the state of cyclic operation, that include heating and cooling blows separated by flow reversals, or flushing phases [20, 21]. As shown in (a) of Fig. 1.3, cold working fluid at a temperature of T_C completely passes through the regenerator and is heated by the regenerator matrix to T_{Reg}. Then, the regenerated working fluid undergoes a thermodynamic process resulting in a temperature of T_H. After which, as shown in (b) of Fig. 1.3, the hot working fluid completely passes back through the regenerator transferring heat to the regenerator matrix and exiting in a cooled state.

A complete analysis of the regenerator would be to determine the temperature behavior of the working fluid for the state of cyclic operation; this demanding task is considered one of the most difficult engineering challenges [22]. However, regenerator effectiveness, which is a dimensionless parameter similar to the typical heat exchanger effectiveness, is a description of a regenerator's quality useful for air-standard cycle analyses, which are focused on thermodynamics only [18, 23]. The parameter can be defined using the heating blow as

$$\epsilon = \frac{\text{Actual enthalpy change of the heating blow}}{\text{Theoretical maximum enthalpy change of the heating blow}}. \tag{1.1}$$

By using the air-standard assumptions that the working fluid is an ideal gas with a constant specific heat, we can write the above, with the notation from Fig. 1.3, as

$$\epsilon = \frac{T_{Reg} - T_C}{T_H - T_C}. \tag{1.2}$$

Organ, an authority on regenerator and Stirling engine analysis, presented Hausen's once accepted regenerator parametric analysis which was an attempt to provide a set of design criteria for the regenerator [22]. The parametric analysis considered the following parameters:

- regenerator effectiveness;
- the number of transfer units, which is a dimensionless parameter relating the regenerator's geometry and heat transfer properties;
- the flushing ratio, which describes the resident working-fluid mass in the regenerator;
- and the reduced period, which is a dimensionless parameter relating the number of transfer units and the flushing ratio.

This analysis is limited by the model used for the heat transfer between the regenerator and the working fluid during the state of cyclic operation. Validations of such models have been attempted, without success, by using data gathered from experiments that considered only a heating process that was similar to the heating blow [20]. Organ stated that Hausen's analysis is in error by orders of magnitude and that design criteria for the regenerator accounting for all aspects of regeneration are still not understood. He presented the complexity of regenerator and Stirling engine design in references [21, 22].

Even though the behavior of an operating regenerator is not fully understood, there are several useful considerations for the design of a practical regenerator. To minimize the temperature variation of the matrix during operation, the heat capacity of the matrix should be much greater than that of the working fluid. This could be accomplished by using a regenerator with a high specific heat and mass. Drag in the regenerator must be minimized, for it reduces both the pressure ratio and the peak operating speed of an engine. This can be accomplished with a short regenerator

having a highly porus matrix. Dead space in the regenerator reduces the pressure ratio of an engine and causes a reduction in performance; it could be minimized by using a dense matrix. Lastly, to preserve the temperature gradient along the length of the regenerator, conduction should be minimized in the direction of fluid flow. This could be accomplished with a long regenerator made of stacked materials that have a low directional thermal conductivity due to contact resistance. These considerations are useful to provide some understanding of regenerator design, but it should be emphasized all can not be satisfied by one particular regenerator [20].

Currently, below the 50 W scale, the efficiency of operable heat engines is at best poor; and the class for small power applications is still dominated by batteries [2]. Nevertheless, the allure of efficient dual-purpose heat engines, that is devices with an ability to generate both mechanical and electrical power, and the high energy density of hydrocarbon fuels still drives the development of small-scale engines. None of the small-scale engine concepts discussed here incorporate regenerative heat exchange, which could potentially better their performance. Recuperators, which are steady state heat exchangers, could be incorporated into small-scale engines where the thermodynamic processes are spatially separated: both small-scale Wankel and small-scale turbine engines could benefit. Different from recuperation, regeneration, which is the beneficial transfer of heat between temporally separated thermodynamic processes, could benefit several engine concepts. Although it is technically challenging, regeneration could be incorporated into small-scale reciprocating engines and engines like the MICE and the MICSE.

1.3 Scope of the Work

This thesis develops a concept for an efficient miniature reciprocating engine for portable power production that, unlike any other known concept with similar requirements, incorporates regenerative heat exchange. This work is based upon research in which the following tasks were completed:

- conception of a regenerated engine with an autonomously-reciprocating regenerator;
- development of a model for the motion of the regenerator;
- design and fabrication of a miniature atmospheric engine simulator;
- and experimentation with the engine simulator to examine the motion of the regenerator and to test the performance of a unique piston-cylinder set.

Simplicity was always held as the central design requirement. Furthermore, it motivated all contributions to the concept: a simple design could reduce the relative size of friction surfaces and lead to success on the small scale, where no successful designs exist.

The proposed engine concept emanated from the rudimentary vapor-compression power cycle known as the atmospheric cycle, which lacks a compression stroke. Although inefficient and ill-suited for large-scale power production, the atmospheric engine could benefit from regenerative heat transfer; moreover, the simple operation is well-suited for miniaturization. In Chapter 3, the thermodynamic basis for this idea is presented. Following from thermodynamics, the operation concept for the miniature reciprocating engine will then be presented with the key element being the motion of the regenerator. Researchers have developed many concepts that incorporate regeneration into reciprocating internal combustion engines; this is discussed in Chapter 2, which is a summary of the literature review. However, none of these regenerated engine concepts have targeted small-scale applications.

A novel aspect of the proposed engine is the actuation of the regenerator. Magnets were incorporated to autonomously actuate the regenerator using the piston. As a

step toward a working engine, a dynamic model for the motion of the regenerator was developed so a mock engine, known as the miniature atmospheric engine simulator, could be created. The dynamic model is also important for the future of the concept. The feasibility of regeneration in an internal combustion engine can only be inspected with thermal modeling once the dynamics of both the working fluid and the regenerator are understood. In Chapter 4, the dynamic model is developed and presented. For the equations of motion to be determined, the dynamic model required considerable experimentation with magnets; these experiments are presented in Chapter 5.

The miniature atmospheric engine simulator was developed concurrently with the dynamic model. As discussed before, simplicity was emphasized; and lubrication-free components were chosen. Of these components, the most unique was a graphite-glass piston-cylinder set that used a clearance seal. In Chapter 6, the design of the engine simulator is presented.

The engine simulator was then used to examine the motion of the regenerator and to test the performance of the graphite-glass clearance seal. As shown in Chapter 7, data from stop-motion photographs were compared with simulations to examine the motion of the regenerator and to successfully validate the dynamic model. The engine simulator was also used to test the performance of the graphite-glass clearance seal. Two types of experiments, which are discussed in Chapter 8, were performed: the pressure behavior of two types of piston-cylinder sets was inspected for a range of operating speeds and long-duration experiments were performed to inspect the longevity of the graphite-glass clearance seal. Chapter 9 finishes this thesis with conclusions and recommendations for future development of the proposed engine.

2 Progress of the In-Cylinder Regenerated Engine

Conception of the miniature regenerated atmospheric engine required a review of the development of single-cylinder in-cylinder regenerated internal combustion engines. This chapter is a chronological canvass of the related literature spanning thirty years of work to develop concepts and to perform analyses and experiments. On this topic, there has been considerable conceptual development; and when appropriate, patent drawings are shown. Most of the analysis performed on regenerated engines has been based upon air-standard assumptions. As part of the evolution of many concepts, less assumptive models were developed as an attempt to understand the complications related to regeneration. Nevertheless, a successful single-cylinder in-cylinder regenerated internal combustion engine has not been created. This chapter is completed by a summary paragraph of the design considerations that were learned from this review and are necessary for the development of a miniature regenerated atmospheric engine.

Pattas observed that the efficiency of a Stirling engine is limited, in part, by the performance of the engine's external heat exchangers. His observation lead to the invention of an engine, patented in 1973, that was likely the birth of the single-cylinder in-cylinder regenerated internal combustion engine (SCRE) idea [24]. He claimed his concept, in which all thermodynamic processes would occur in one cylinder, would produce a higher peak cycle temperature than Stirling engines of the time and in turn be more efficient. The drawings from the patent show a single-cylinder engine with a regenerator situated between two opposed pistons, with an undisclosed motion designed for optimal regeneration.

Nearly a decade after Pattas's invention, Millman patented an engine with a moving regenerator [25]. The concept was similar to conventional internal combustion engines except it had a regenerator between the piston and the top of the cylinder. In the concept, regeneration would be timed by the regenerator's undisclosed motion, which would be effected by a mechanism that would couple the regenerator to the piston at particular moments of the cycle. Millman claimed the conceptual engine's regenerative cycle would be optimal at a low compression ratio which would allow dead space for the regenerator and internal engine mechanisms. A drawing from the patent is displayed in Fig. 2.1 showing an internal mechanism to couple the regenerator and the piston.

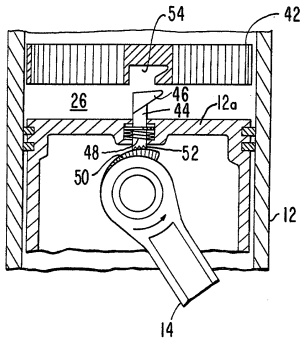

Figure 2.1: A drawing from Millman's 1981 patent showing a mechanism for coupling the regenerator and the piston [25].

In works starting in 1982, Keating and Pouring presented parametric air-standard analyses of the regenerated Otto and the regenerated Diesel cycles [26, 27]. The motivation for these analyses was the same as Pattas's: heat transfer in external heat exchangers limits the performance of Stirling engines. Assumptions for these analyses were based upon a concept with a regenerator that protruded from the surface of the piston. For the analyses, the regenerator was considered a thermal reservoir with a constant temperature that was used to define the regenerator effectiveness. These analyses showed, with perfect regeneration, regenerated cycles having the same compression ratios as the corresponding basic cycles can have higher cycle efficiencies due to both higher peak pressures and peak temperatures. In addition, these analyses indicated that the cycles' efficiencies are sensitive to the following parameters: peak cycle temperature, constant regenerator temperature, external heat addition, regenerator heat addition, and compression ratio.

Isshiki et al. measured the efficiency of possibly the first working SCRE [28]. The engine, which had been in development since 1980, resembled a beta Stirling engine with a regenerator in the usual place of the displacer. During initial trials with the engine, regenerators made of ceramics or stacked stainless-steel mesh were used. However, these regenerators did not withstand the dynamic and thermal loading from operation; it is this failure that revealed regenerator design as a stifling challenge. Thus, robust regenerators made of cast iron and and nickel-chromium foam were used to complete the experiments, which had limited success. The efficiencies measured were low, and the authors believed mechanical losses and poor regenerator performance were responsible. A summary of the engine's performance, with it running on either gasoline or diesel fuel, is presented in Table 2.1.

Moriya et al. continued Isshiki's work and modified the engine into an apparatus to characterize regenerators [29, 30]. Both the regenerator effectiveness and the pressure drop across the regenerator were measured for regenerators made from the following materials: stacked stainless-steel mesh, silicon-carbide spheres, and nickel-chromium foam. The experiments showed regenerator effectiveness decreases with increased engine speed and the pressure drop across the regenerator increases with increased flow through the regenerator. These conclusions suggest the addition of a regenerator to an internal combustion engine will limit operation speed. For engine speeds between 700 rpm and 1000 rpm, the stacked stainless-steel mesh regenerator had a regenerator effectiveness, exceeding the other materials, above 90 %.

Pavletič et al. published a paper that presented a parametric air-standard analysis of the regenerated Otto cycle and a SCRE concept [31]. The analysis, unlike Keating and Pouring's, treated the regenerator effectiveness as a parameter. It was shown that the regenerated Otto cycle has a higher cycle efficiency at a comparably lower compression ratio than the basic cycle. The engine concept presented was not entirely new; it resembled Pattas's engine. However, unlike Pattas's patent a detailed description of the motion of both of the pistons along with critical engine dimensions was disclosed. The authors claimed the conceptual engine would not require an ignition system because the regenerator would cause combustion of the fuel-air charge by providing enough heat for autoignition.

Table 2.1: Performance of Isshiki's experimental engine [28].

	Gasoline	**Diesel Fuel**
Regenerator Material	Cast Iron	Nickel-Chromium Metal Foam
Engine Speed, rpm	1000	600
Indicated Efficiency	15 %	35 %
Measured Efficiency	6 %	5 % to 7 %

In 1988 two concepts, which were further developed for at least the following decade, were patented by Ferrenberg and Webber, who were motivated to develop a simple embodiment of a SCRE [32, 33]. Both of the conceptual engines, conceived to operate using two-stroke or four-stroke cycles, were based upon a moving regenerator located between the piston and the top of the cylinder. The idea was similar to Millman's except the regenerator's motion, which was disclosed, would be caused by an external mechanism. The difference between Ferrenberg and Webber's two concepts was the location of the hot space as shown by Fig. 2.2, which displays the cold-piston concept with the hot space located above the regenerator, and Fig. 2.3, which displays the hot-piston concept with the hot space located below the regenerator. These concepts were further explained in Ferrenberg's 1990 article where he discussed design considerations and provided a thermodynamic basis using air-standard analyses of the regenerated Otto and regenerated Diesel cycles [34, 35]. In agreement with Isshiki, Ferrenberg considered the regenerator's design to be the largest problem confronting successful development of a SCRE with a moving regenerator. This is because the regenerator must withstand high temperatures, rapid temperature fluctuations, and dynamic loads. Ferrenberg described several ideas for reinforced ceramic regenerators that might overcome the challenge.

Ferrenberg et al. recognized the limitations of air-standard analyses and developed a more realistic model to aid in the design of the aforementioned cold-piston SCRE [36]. For the model, which was specific to a two-stroke cycle, the volume contained by the engine cylinder and regenerator were treated as several discrete volumes where conservation of both mass and energy were upheld. The model was implemented as a time-marching program, named the REGEN model, that provided a solution depending on a combustion heat-release profile and known kinematics of the piston and the regenerator. Unlike the air-standard analyses, the REGEN model showed that the regenerator's cooling stroke should start during the last half of the expansion stroke. This conclusion emphasized the importance of both the regen-

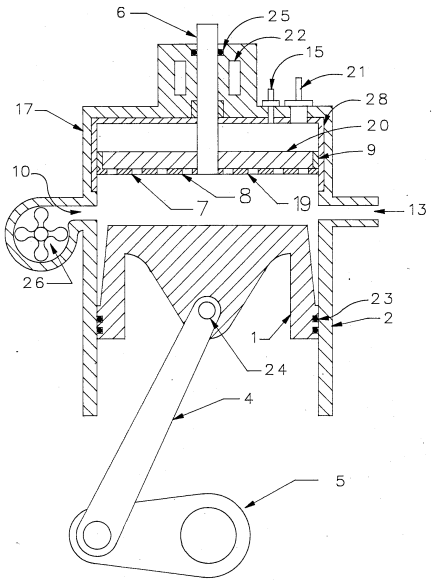

Figure 2.2: A drawing from Ferrenberg and Webber's 1988 patent showing a concept for a cold-piston SCRE [32].

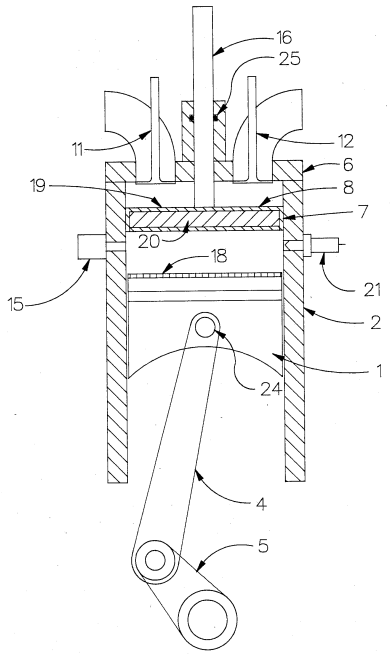

Figure 2.3: A drawing from Ferrenberg and Webber's 1988 patent showing a concept for a hot-piston SCRE [32].

erator's motion and the timing of regeneration. The results from the model were compared to measured data from a turbocompounded low-heat-rejection diesel engine; the model predicted that a cold-piston SCRE of similar size operating at half of the diesel engine's compression ratio would provide 30 % more power at a 10 % increase in efficiency. Ferrenberg noted that a real engine, as indicated by the model, would have a high peak temperature and likely produce nitrogen oxides, a known pollutant. He commented that the combustion environment of the engine, which was not understood, was different from conventional engines and that prediction of the severity of this problem was difficult.

Regenerators made of new materials, for the time, were researched by Ferrenberg and Williams [37]. These regenerators were constructed using chemical-vapor-deposition formed foams made with either silicon-carbide, silicon-nitride, or niobium and were successfully subjected to structural tests at 1700 rpm and 1000 °C for tens of minutes without failure. Patents reflecting these novel regenerators and modifications to the regenertor's motion based upon findings from the REGEN model were awarded to Ferrenberg in 1995 and 1997 [38, 39].

About when Ferrenberg patented his first concepts, Ruiz presented concepts for SCREs based upon parametric air-standard analyses of the regenerated Otto, regenerated Diesel, and regenerated atmospheric cylces [40–42]. These concepts differed from Ferrenberg's because none of them incorporated an independently moving regenerator. In Ruiz's concepts, flow of the working fluid would be controlled by a free piston located between the piston and the top of the cylinder. The concepts were divided into two categories: flat-piston and bowl-piston. The flat-piston concepts had a stationary regenerator; the bowl piston concepts, however, had a regenerator that was part of a ring fixed to the top of the piston. For both engine categories, the motion of the piston would cause the free piston to direct the working fluid through the regenerator during particular periods of the cycle. Ruiz, like Pavletič, believed that for some of the concepts heat from the regenerator would cause autoignition of

the fuel-air charge; if practical, this feature would allow for a simple engine design. In addition, he commented that peak engine speeds would be limited by drag caused by the regenerator and the dynamics of the free piston.

Ruiz's parametric air-standard analyses showed that the addition of regeneration to the Otto and Diesel cycles produces a significant increase in cycle efficiencies, which is maximized at an optimal compression ratio; the analyses also showed it is the atmospheric cycle that benefits the most from regeneration, which can more than double in cycle efficiency. Because of these promising results, Thyageswaran and Ruiz presented a time-dependant analysis of a regenerative engine cycle that accounted for fluid flow through the regenerator and heat transfer between the regenerator and the working fluid [43]. This stronger analysis had similar conclusions and showed that a regenerated engine would have an increased thermal efficiency when compared to conventional engines and the optimal efficiency would occur at a comparably low compression ratio.

Clarke was also active in the development of SCRE concepts. In his 1990 article, he presented air-standard analyses of the regenerated Otto, regenerated Atkinson, and regenerated full-expansion cycles that showed, for all of these cycles, increased cycle efficiency or reduced peak pressure could be attained by using regeneration [44]. Later, in 1996, he patented a concept for a SCRE similar to Ferrenberg's cold piston concept [45]. Clarke's patent, however, presented the idea of introducing a cooling liquid into the intake stream. He claimed the cooling liquid would improve performance for two reasons: the heat transfer rate from the regenerator would be increased by reducing the temperature of the intake air; the required compression work would be decreased because of the cooling liquid's phase transformation during the compression stroke. Clarke patented another concept for a SCRE in 2003 [46]. As shown in

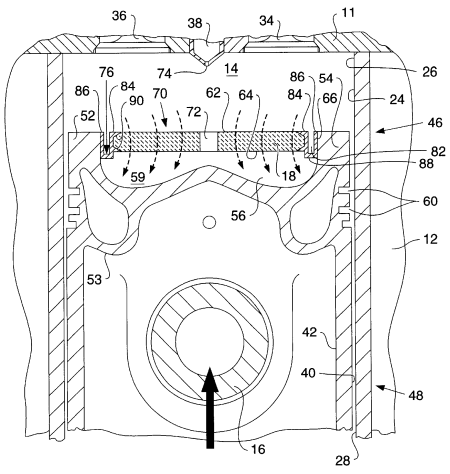

Figure 2.4: A drawing from Clarke's 2003 patent showing a concept for a SCRE where the regenerator is part of the piston [46].

Fig. 2.4, the regenerator is part of the piston; and heat addition from the regenerator would occur during the entire compression stroke. At the end of the compression stroke, the regenerator would mate with the fuel injector and combustion would take place in a cavity inside the piston following fuel injection.

Two more patents of SCREs are worth noting. Warren stated that past concepts failed because they were adaptations of conventional engines that didn't properly use a regenerator [47]. His concept, as shown in Fig. 2.5, included a complicated displacer-regenerator with internal valves that would optimize regenerative heat transfer during both the intake and exhaust strokes. In Lowi and Ferrenberg's 2003 patent, they stated that past concepts were not based upon models of appropriate sophistication and failed because heat transfer between the regenerator and the working fluid was not occurring at optimal times [48]. A concept, with an opposed two-piston configuration similar to Pattas's concept, was presented that was conceived from insight provided by an undisclosed model; the concept is shown in Fig. 2.6. Lowi claimed the pistons's motions were near the optimal motions computed by the model.

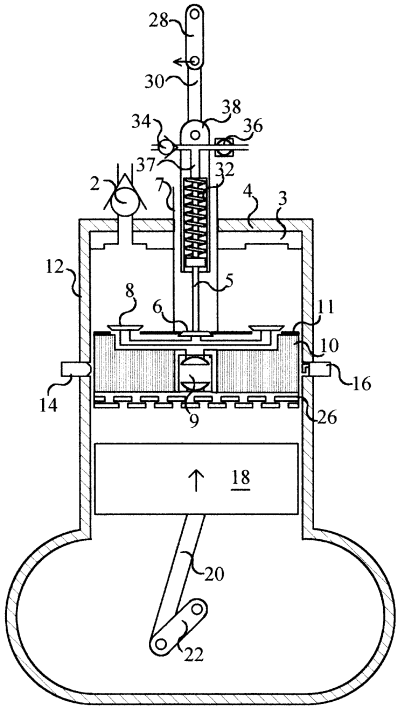

Figure 2.5: A drawing from Warren's 2000 patent showing a concept for an SCRE with a displacer-regenerator [47].

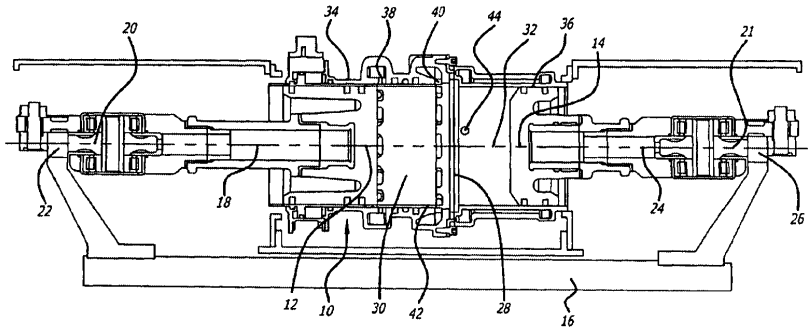

Figure 2.6: A drawing from Lowi's 2003 patent showing a concept for an SCRE with opposed pistons and a stationary regenerator [48].

Several design considerations were learned from this literature review and are necessary for the development of the miniature atmospheric engine. The addition of a regenerator to an internal combustion engine creates significant complications: higher peak temperatures cause material selection for several engine components to be of concern; the regenerator must withstand high temperatures, rapid temperature fluctuations, and, if motion is required, dynamic loads. Due to drag, the regenerator will also limit engine operation speed. Simplicity of design is always a consideration and, depending upon the engine, the regenerator may improve simplicity by having a second purpose as an igniter. Air-standard analyses showed that many concepts can theoretically have an increased cycle efficiency due to regeneration, particularly the atmospheric cycle. The more sophisticated models presented, however, revealed that an understanding of the timing of the heat transfer between the regenerator and the working fluid is necessary for creation of a successful SCRE. Moreover, development of such models require a particular concept to be used for optimization; that is, no model exists that can determine the optimal configuration of a SCRE.

3 Concept for a Regenerated Atmospheric Engine

The atmospheric engine was abandoned due to its low efficiency. However, its simple design is ideal for miniature applications, and an air-standard thermodynamic analysis indicates that an atmospheric engine could greatly benefit from regeneration. In this chapter, the concept for the regenerated atmospheric engine is presented along with a promising air-standard analysis. From this analysis, it is shown that the air-standard thermodynamic cycle has two unique features. First, the addition of a marginally effective regenerator could result in a tremendous increase in thermal efficiency. Second, the cycle is exceptionally sensitive to regenerator effectiveness over large windows of both temperature ratio and expansion ratio. Following these ideas, the ideal concept of operation, with the key element being the motion of the regenerator, is presented. This chapter then concludes with a discussion of this concept in the context of single-cylinder in-cylinder regenerated internal combustion engines.

3.1 Regenerated Atmospheric Cycle

The atmospheric engine sparked the age of internal combustion power. The first of which was developed by a Swiss engineer, Rivaz, who wished to build a self-powered cart and was successful during 1805 using a crude atmospheric engine. Following this success, many engineers began development of atmospheric engines; and in 1867, Otto and Langen introduced an atmospheric engine which in the coming years was proven as the standard for suitable industrial applications [49]. Atmospheric engines were soon replaced by higher-performance four-stroke engines employing mechanical gas compression and there has been little development since [50].

Engines based upon the atmospheric cycle were abandoned because of their low efficiency. However, a thermodynamic analysis of the air-standard regenerated atmospheric cycle reveals an exceptional sensitivity to regenerator effectiveness for the practical ranges of temperature ratio and expansion ratio. This analysis suggests it may be possible to develop a high-performance regenerated atmospheric engine.

Figure 3.1 displays a P-V diagram for the regenerated atmospheric cycle. It is comprised of three processes in the following sequence: constant-volume heat addition ($1 \rightarrow 2$), where a portion of the added heat comes from regeneration; isentropic expansion ($2 \rightarrow 3$); and constant-pressure heat rejection ($3 \rightarrow 1$). In previous work,

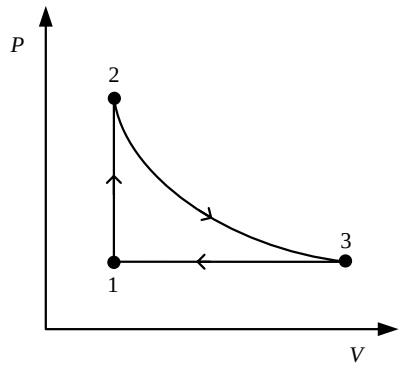

Figure 3.1: A P-V diagram for the air-standard regenerated atmospheric cycle.

Ruiz presented a parametric air-standard analysis of this cycle [41]. He defined the thermal efficiency as

$$\eta = \frac{1/\tau - 1 - k\left(\tau^{-1/k} - 1\right)}{1/\tau - 1 - \epsilon\left(\tau^{-1/k} - 1\right)}, \tag{3.1}$$

where the regenerator effectiveness is defined as

$$\epsilon = \frac{T_2' - T_1}{T_3 - T_1}. \tag{3.2}$$

Concerning ϵ, T_2' is the temperature attained after regeneration alone. Using the equation of state and the definition of an isentropic process for an ideal gas with constant properties, the expansion ratio is defined by

$$r = \tau^{-1/k}. \tag{3.3}$$

In Fig. 3.2, thermal efficiency is plotted separately as a function of temperature ratio and expansion ratio. These plots were created using Eqs. (3.1) and (3.3) with $k = 1.4$. For any pair of τ and r, we can observe that the thermal efficiency significantly increases with regenerator effectiveness. As an example, let $k = 1.4$ and $\epsilon = 0.75$. For $\tau = 0.1$, the thermal efficiency increases from 35 % to 54 % with regeneration; and, with $\tau = 0.25$, it increases from 21 % to 36 %. Both of these cases represent a significant increase in thermal efficiency.

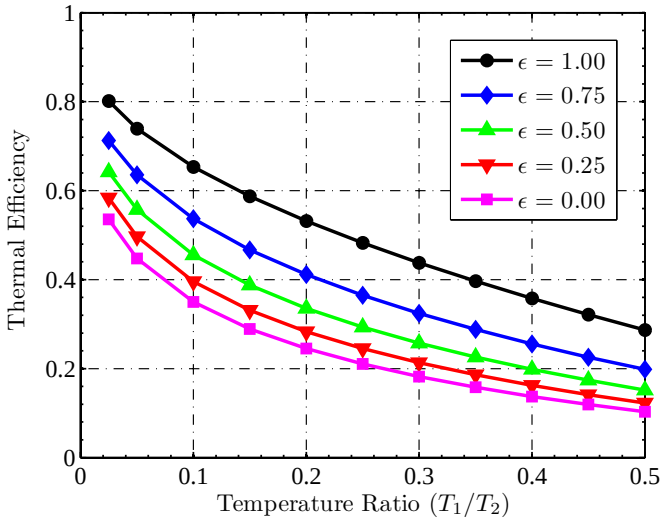

(a) Thermal efficiency as a function of temperature ratio.

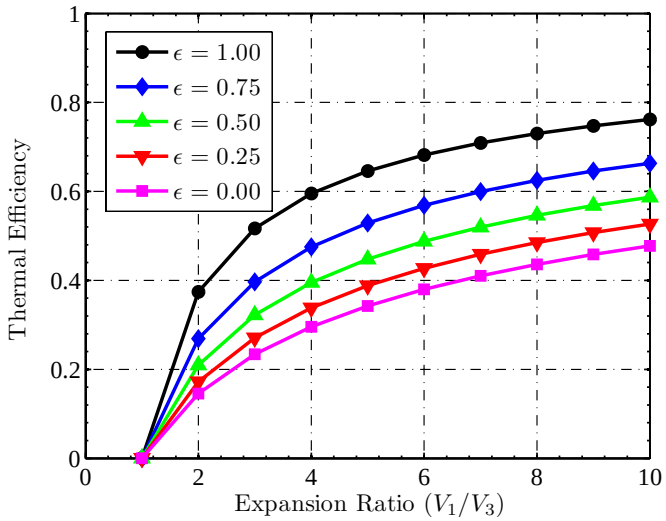

(b) Thermal efficiency as a function of expansion ratio.

Figure 3.2: Plots of thermal efficiency as a function of temperature ratio and thermal efficiency as a function of expansion ratio both with $k = 1.4$.

3.2 Atmospheric Engine with In-Cylinder Regeneration

Thermodynamic analysis has established the possibility of high-performance regenerated internal combustion engines, yet there are no successful designs to date [37, 41]. A complication for many conceived engines is that the fuel-air charge expands prematurely when in the neighborhood of the regenerator during the compression stroke [51]. The atmospheric engine is unique; it lacks a compression stroke. Thus, in-cylinder regeneration in an atmospheric engine should not attenuate the cycle.

Because of the simplicity of atmospheric engines and the conclusions from Ruiz's air-standard analysis, a concept for the ideal operation of a regenerated atmospheric engine that is suitable for a miniature embodiment was developed. This proposed regenerative engine relies on the location of the regenerator to time regeneration. During intake, the regenerator and piston are coupled to prevent flow of the fuel-air charge through the regenerator. The couple between the piston and the regenerator is imperative: it serves as a valve to time regeneration; when the pair separates, regeneration begins. Ignition of the fuel-air charge could occur from either autoignition due to a sufficiently high regeneration temperature or a catalytic combustor that is part of the regenerator [41]. Figure 3.3 shows the ideal operation of the proposed engine, which is explained below. Each segment of the ideal operation corresponds to the air-standard cycle, where the constant-pressure heat rejection represents $3 \rightarrow 1'$ and $1' \rightarrow 1$. Note that in an actual cycle, the continuous motion of the piston will cause the following segments to blend together.

1 With the intake and exhaust valves closed, a fuel-air charge is present; and the piston and regenerator are coupled.

1 → 2 After the regenerator and piston separate, the regenerator moves upward heating the fuel-air charge at constant volume; the fuel-air charge combusts.

2 The regenerator arrives at the top of the cylinder as the heat addition is completed.

2 → 3 The hot-gas charge expands as the piston moves downward.

3 The piston arrives at bottom dead center.

3 → 1′ With the exhaust valve open, the piston moves upward purging the exhaust from the cylinder.

1′ The piston and regenerator couple at top dead center.

1′ → 1 With the intake valve open, the piston and regenerator move downward drawing in a new fuel-air charge.

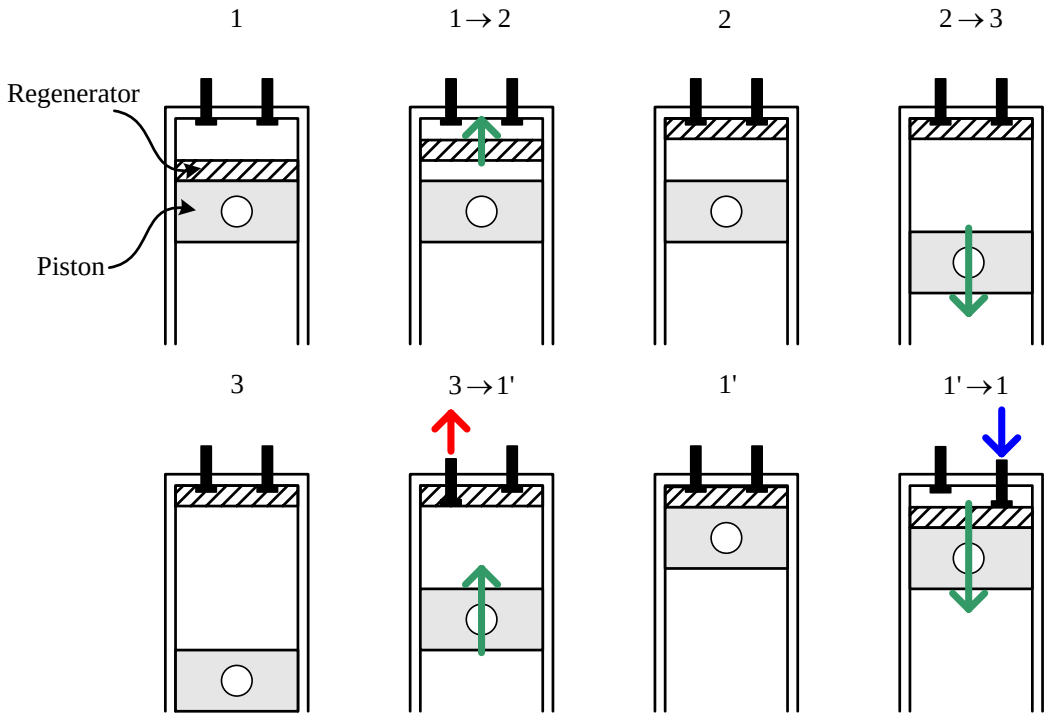

Figure 3.3: Segments of the ideal operation of the proposed regenerative engine.

The concept presented here has similarities to some of those encountered while researching the development of SCREs; a summary of this research can be found in Chapter 2. Like most of the SCRE concepts, the proposed regenerative engine utilizes a regenerator that would transfer heat to the working fluid at a particular time. Furthermore, this heat transfer would be determined by the particular motion of the regenerator. Like Millman's concept, this concept utilizes a couple between the regenerator and the piston to time regeneration. In contrast, however, a complicated mechanical linkage was avoided: it was decided the couple would be simply provided by a pair of magnets. Like Ferrenberg and Webber's hot-piston concept, the combustion region is between the regenerator and the piston. The concept of this proposed engine emanated from the atmospheric cycle which has lead to a subtly different incarnation of a two-stroke engine. To the author's knowledge, this concept is novel because, unlike others, it incorporates regenerative heat exchange on a small scale.

4 Development of the Dynamic Model

A dynamic model for the motion of the autonomously-reciprocating regenerator was developed concurrently with the miniature atmospheric engine simulator and was created for two purposes. First, completion of the design for the engine simulator required it. And second, the feasibility of this particular concept for a miniature regenerated atmospheric engine can only be inspected with thermal modeling once the dynamics of the regenerator are understood. This chapter is a development of the dynamic model and starts with a presentation of a concept for a mechanism resembling the ideal operation developed in Chapter 3. Then, the motion of the regenerator is divided into four phases where Newton's method is separately applied to develop equations of motion. Following, the regenerator's drag force and the force due to the pressure difference across the regenerator are developed using the Darcy friction factor. This chapter does not include the development for the magnetic attraction force, which required considerable experimentation.

4.1 Concept for the Dynamic Model

The dynamic model and the miniature atmospheric engine simulator were developed concurrently. Before developing the dynamic model, a mechanism was conceived with the intent of it having a cyclical motion resembling the ideal operation presented in Section 3.2. Figure 4.1 shows a schematic of the externally-actuated conceptual mechanism. Magnets cause the piston and regenerator to couple until separation occurs because of the keeper meeting the stop. Then, a return spring draws the regenerator back to the top of the cylinder completing a procession causing autonomous motion of the regenerator.

This is a concept for a hot-piston engine. Namely, the combustion region would be between the piston and the regenerator. Combustion temperatures would be higher than the Curie temperature of the magnets, which is where magnetization is lost. For this reason, the magnets in a practical engine would be thermally isolated from the hot zone. However, the simple concept shown is convenient for creating a prototype.

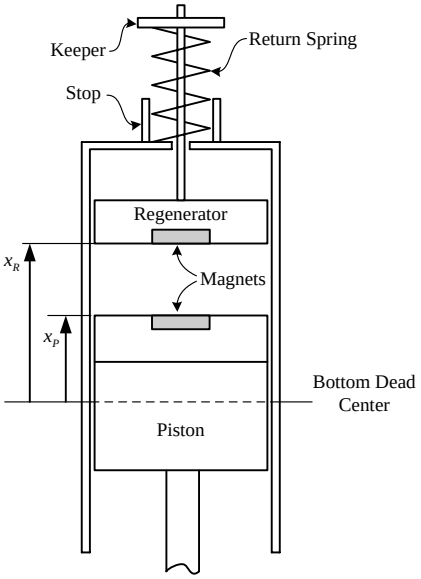

Figure 4.1: The conceptual mechanism for the dynamic model.

4.2 Motion of the Regenerator

The motion of the regenerator is different for each segment of operation. For the model, periods of uniform motion are considered phases, which are explained below.

Top Dwell The regenerator rests at the top of the cylinder.

Interaction Body forces cause the regenerator to move freely.

Coupled The regenerator is coupled to the piston, which defines the motion of the pair.

Bottom Dwell The regenerator rests at the bottom of its travel.

Figure 4.2 shows free body diagrams of the regenerator for each phase. The model neglects sliding friction and accounts for magnetic attraction, return spring force, drag, and pressure difference across the regenerator. During the top and bottom dwell phases, the regenerator is not moving. Kinematics of the actuated piston, which are a characteristic of the engine simulator's drive mechanism, define the motion for the coupled phase. The interaction phase, however, requires an equation of motion. Summing the forces on the free body diagram and equating them to $m\ddot{x}_R$ defines this equation as

$$m\ddot{x}_R = F_P + F_S - F_V - F_M - mg. \tag{4.1}$$

Events initiate a shift between phases and are described in Table 4.1; their relationship with the phases is shown in Fig. 4.3. Each event is flagged by either the location of the regenerator or the absence of a particular body force (F_{Top}, $F_{Coupled}$, or F_{Bottom}). For example, if the piston and regenerator are coupled and $F_{Coupled}$ becomes zero then event C1 is flagged. As a result, the regenerator's motion is shifted to the interaction phase.

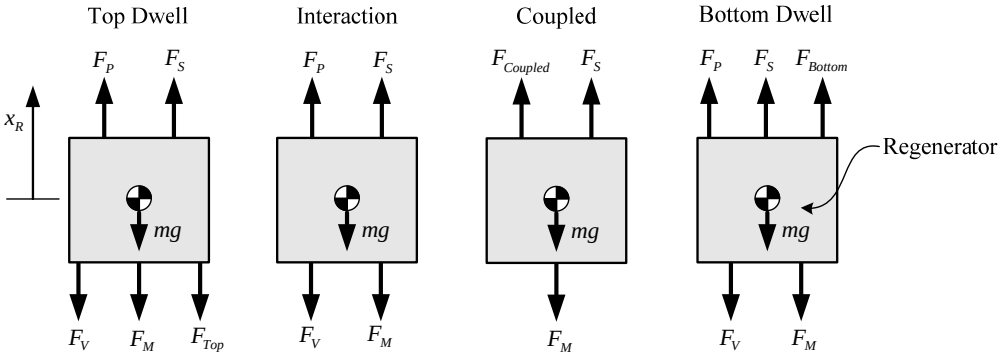

Figure 4.2: Free body diagrams of the regenerator for each phase of motion.

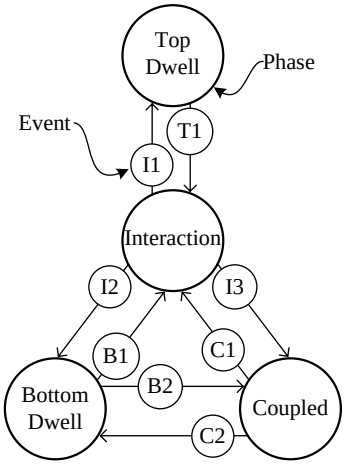

Figure 4.3: The relationship between the events and phases.

Table 4.1: Description of the events.

Event	Description
T1	$F_{Top} = 0 = F_S + F_P - F_M - F_V - mg$
I1	The regenerator reaches the top of the cylinder.
I2	The regenerator reaches the bottom of its travel.
I3	The regenerator and the piston meet.
C1	$F_{Coupled} = 0 = F_S - F_M - mg - m\ddot{x}_P$
C2	The regenerator reaches the bottom of its travel.
B1	$F_{Bottom} = 0 = F_S + F_P - F_M - F_V - mg$
B2	The regenerator and the piston meet.

4.3 Drag and Pressure Forces

The dynamic model requires forces for the drag, F_V, and the pressure difference across the regenerator, F_P. To derive equations representing these forces, we must assume a geometry for the regenerator. A regenerator with a simple geometry, a dummy-regenerator, was conceived for modeling purposes; and both of these forces are represented by a coefficient of the velocity of the fluid flowing through this model-specific regenerator, which is displayed in Fig. 4.4. Each force is derived using the regenerator's geometry and the Darcy friction factor.

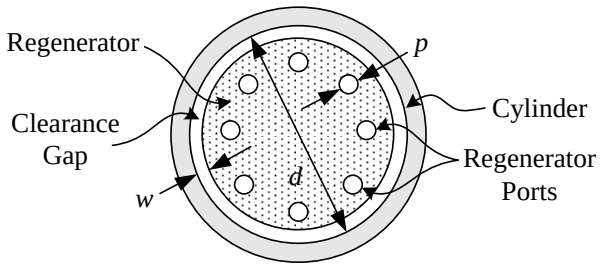

Figure 4.4: A top view of the dummy-regenerator.

First, the drag force will be developed. Fluid flow through the clearance gap and regenerator ports are treated in a similar manner, but separately considered. Using the conservation of mass and assuming the fluid to be incompressible, we can define a velocity amplification factor using the surface areas normal to the flow as

$$\alpha = \frac{d^2}{np^2 + 4\left(wd - w^2\right)}, \tag{4.2}$$

where n is the number of regenerator ports. The fluid flow through the regenerator is assumed to be at steady state, fully developed, and laminar. Using the Darcy friction factor as defined by White, we can define the force acting on the regenerator for fluid flow through the clearance gap as

$$F_{V,Gap} = \frac{4\pi\mu H\alpha\left(\dot{x}_R - \dot{x}_P\right)(d-2w)}{w}, \tag{4.3}$$

where H is the height of the regenerator [52]. Equation (4.3) requires computation of the hydraulic diameter. For this, it is assumed that $w << d$ so that the calculation can be simplified. The drag force for fluid flowing through the regenerator ports is also found using the Darcy friction factor. It is defined by

$$F_{V,Ports} = 8\pi\mu H\alpha n\left(\dot{x}_R - \dot{x}_P\right). \tag{4.4}$$

Combining Eqs. (4.3) and (4.4) and rearranging to form $F_V = C_V\left(\dot{x}_R - \dot{x}_P\right)$ yields

$$C_V = 4\pi\mu H\alpha\left[\frac{(d-2w)}{w} + 2n\right]. \tag{4.5}$$

The force for the pressure difference across the regenerator must also be considered. As an additional assumption, the top side of the regenerator is always exposed to atmospheric pressure. This means the region above the regenerator is constantly at atmospheric pressure. Although this assumption is not representative of an actual engine, it allowed an account of the pressure-difference force using the Darcy friction factor. The force for the pressure difference can be written as

$$F_P = \frac{32\mu H\alpha A\left(\dot{x}_R - \dot{x}_P\right)}{p^2}, \tag{4.6}$$

where A is the surface area of the regenerator normal to the flow and is defined as

$$A = \frac{\pi}{4}\left[(d-2w)^2 - np^2\right]. \tag{4.7}$$

Rearranging the above to form $F_P = C_P\left(\dot{x}_R - \dot{x}_P\right)$ yields

$$C_P = \frac{32\mu H\alpha A}{p^2}. \tag{4.8}$$

5 Magnet Characterization

The dynamic model requires a continuous function representing the magnetic attraction force. The pole model could be used for this purpose; but without an accurate estimation of certain magnet constants, it is a poor representation. Therefore, a function was created using experimental data. In this chapter, the experimental methods used to characterize a pair of magnets and the results are presented. Magnetic attraction force data for a pair of magnets and for a magnet and a steel sample were collected using a custom apparatus. The characterization was then completed using an algorithm to fit the data with the inverse-square law.

5.1 Experimental Methods

One input to the dynamic model is the magnetic attraction force, F_M. The pole model, a relationship developed by assuming the attraction force acts at a magnet's pole, can be used to estimate this force as a function of distance. This model requires constants that are difficult to measure. In previous work, McCaig and Gould discussed ambiguities associated with this model and its considerable departure from experimental data [53, 54]. For these reasons, the pole model was not used. It has been shown, however, that the inverse-square law can model the force between two magnets [55, 56]. Thus, experimental data were used to determine a function for F_M specific to a particular pair of magnets. Cylindrical neodymium magnets (K and J Magnetics, Inc. model D31) were chosen for characterization by considering their thickness, diameter, and published holding force which were 1.6 mm, 4.8 mm, and 9 N, respectively.

5.1.1 Apparatus

The D31 magnet was characterized using a test apparatus (Fig. 5.1) consisting of a vertical aluminum c-frame that maintained alignment of a load cell, the test specimens, and a dial indicator using plastic threaded rod. The throat of the c-frame was large enough to ensure magnetic components were at least 7 cm, a distance determined not to affect the experiment, from the magnets. The magnet test specimens were made by affixing the magnets to threaded plastic cylinders with epoxy; the specimens were carefully fabricated to ensure the magnets would be coaxial with the threaded rods. A threaded cylindrical 1018 steel test specimen was also made and had the same dimensions as the magnet test specimens. Several of the components used for the characterization are listed in Table 5.1.

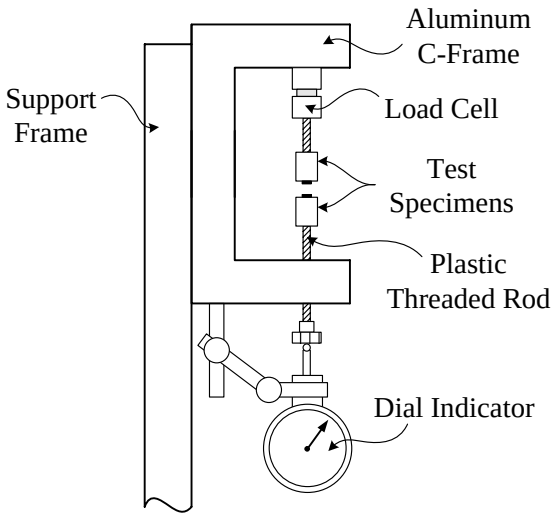

Figure 5.1: A schematic of the test apparatus used to characterize the magnet.

5.1.2 Procedures

Two types of experiments were performed: attraction force for two magnets and attraction force for a magnet and a 1018 steel sample. Because the magnetic attraction force is sensitive at small separation distances, effort was made to account for variability among the magnets and to reduce the precision error for the uncertainty analysis. Thus, nine pairs of magnets were used for the two-magnet experiment; and three magnets were used for the magnet-steel experiment. In addition, seven runs were performed for one pair of magnets and for a magnet and a steel sample so precision error could be accounted for in the uncertainty analysis.

Table 5.1: Several of the components used to characterize the D31 magnet.

Balance	
Manufacturer	Ohaus
Model Number	Navigator N12120
Serial Number	1121133573
Notes	Resolution ±0.005 g, Linearity ±0.01 g
Uncertainty	$u_B = 1.096 \times 10^{-4}$ N
Computer	
Manufacturer	Dell
Model Number	Optiplex GX620
Serial Number	B7VKY71
Data Acquisition Chassis	
Manufacturer	National Instruments
Model Number	SC235 with SCCPWR02
Serial Number	1116D90
Dial Indicator	
Manufacturer	Aerospace
Serial Number	HT2484
Load Cell	
Manufacturer	Omega
Model Number	LCL-005
Notes	Combined Error = 0.25 % of Full Scale Output, Excitation = 10 V, Rated Output = 2 mV/V
Uncertainty	$u_L = 5 \times 10^{-5}$ V
Signal Conditioning Module for Load Cell	
Manufacturer	National Instruments
Model Number	SCC-SG24
Serial Number	1148EE6

Two-point calibrations for the load cell were performed to complete the experiments. For the following two reasons, the load cell was calibrated each time the upper test specimen was changed: the mass of the test specimens varied, and the load cell's calibration was sensitive to the small deflections required to install the upper test specimen into the test apparatus. Each calibration, which was a linear function relating force to the load cell output voltage, was completed using an average of three no load voltage measurements and an average of three voltage measurements with a 1 kg mass hung from the load cell; both of the voltages were recorded using LabVIEW.

The calibration mass provided a force greater than the published holding force of the D31 magnet and was selected to ensure the data would be between the calibration points.

The runs for both experiments were completed as follows. First, the test specimens were fastened to the threaded rod; and, if required, the load cell was calibrated. Second, the most critical step, the initial separation distance was set using a plastic feeler gauge with a thickness of 0.08 mm; and the dial indicator was zeroed. Finally, the attraction force was measured in increments of 0.25 mm to the maximum separation distance of 12.7 mm, and the results were recorded using LabVIEW.

5.1.3 Data Reduction

The inverse-square law was used to characterize the magnet and is defined by

$$F_M = \frac{k_{Mag}}{(x + h_{Mag})^2}, \tag{5.1}$$

where x is the separation distance. To prevent singular behavior, the constant h_{Mag} shifts the function at $x = 0$. The physical representation of h_{Mag} is the offset of the pole from the face of the magnet [55, 56]. The constants were found iteratively using an algorithm which minimized the residual between the data and the inverse-square law. The algorithm was written in MATLAB and is presented in Appendix B. For reasons which will be discussed, only data from the two-magnet experiment was fit. For each run of the two-magnet experiment, the constants were computed; the average of all of the constants was used to complete the characterization.

The Kline-McClintock method was used to estimate the uncertainty of the data for both experiments [57]. The uncertainty analysis is presented in Appendix A. The uncertainty for the separation distance was neglected because its consideration yielded unreasonable results. These results were caused by the inverse-square law's sensitivity to separation distance. The uncertainty of the magnet characterization was inspected using the dynamic model; this is discussed in Section 6.2.

5.2 Results and Discussion

Figure 5.2 displays plots of the average magnetic attraction force versus separation distance for the two-magnet experiment and the magnet-steel experiment. Comparing the two plots, notice the sharper decrease of the attraction force with separation distance for the magnet-steel data. This difference was expected, for McCaig stated that at a distance a pair of permanent magnets will exert a greater attraction force than a magnet and a piece of steel [53]. For this reason, a pair of D31 magnets was chosen for the engine simulator; and data from the two-magnet experiment were used to create a function for the dynamic model.

The data from the two-magnet experiment were fit using the following constants: $k_{Mag} = 6.52 \times 10^{-6}$ N·m^2 and $h_{Mag} = 7.10 \times 10^{-4}$ m. The fitted function, displayed in (a) of Fig. 5.2, closely represented the data with a maximum deviation of 0.887 N. The value of the fitted function at $x = 0$ disagreed with the published holding force by 41 %. Gould claimed the main difficulty when modeling magnetic forces is the estimation of magnet constants [54]. Moreover, the inverse-square law is sensitive to k_{Mag} and h_{Mag} and unstable near $x = 0$. These matters probably contributed to the disagreement between the fitted function and published holding force.

Although the dynamic model requires a larger domain, the magnetic attraction force for separation distances between 0.5 mm and 3 mm is critical. Between these distances, the fitted function slightly underestimates the force and provides a conservative representation of the data for the dynamic model. The uncertainty of the data was considerable at small separation distances. The inverse-square law is sensitive at small separation distances, and the error in positioning the magnets is a major cause for the considerable uncertainty of the data.

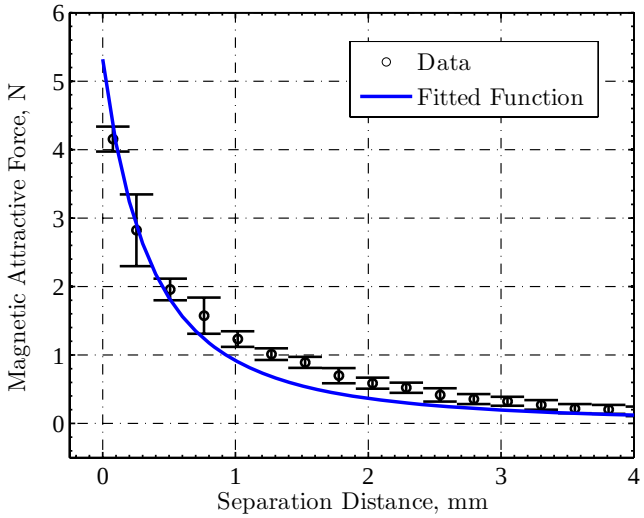

(a) Two D31 magnets.

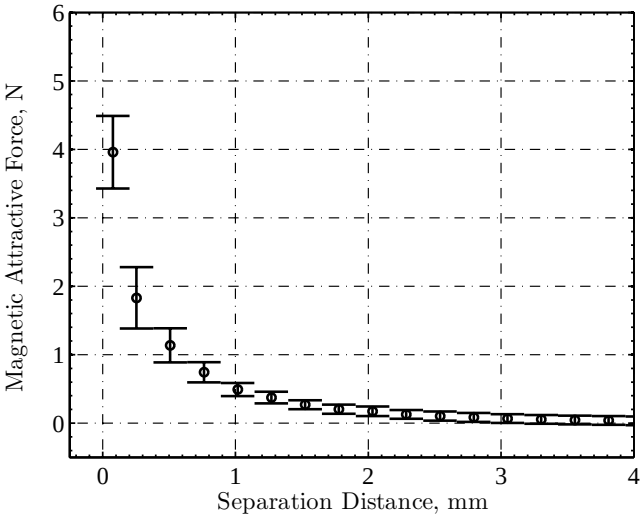

(b) A D31 magnet and a 1018 steel sample.

Figure 5.2: Magnetic attraction force versus separation distance for both experiments. In (a), the fitted function is displayed.

6 Development of the Miniature Engine Simulator

A miniature atmospheric engine simulator was developed concurrently with the dynamic model for two purposes: to examine the motion of the magnet-actuated autonomously-reciprocating in-cylinder regenerator and to test a graphite-glass clearance seal to gain knowledge for future piston scaling studies. This chapter is a development of the design of the engine simulator. The two configurations of the engine simulator are pictured, and detailed schematics are also presented. Simplicity was emphasized during the design process, and lubrication-free components were chosen. Of these components, the most unique was a graphite-glass piston-cylinder set that used a clearance seal. Simulations from the dynamic model are also presented showing the position of both the piston and the regenerator as a function of time. The simulations included represent the final design case and weak pairs of magnets.

6.1 Design of the Miniature Atmospheric Engine Simulator

A miniature atmospheric engine simulator was constructed for two purposes: to examine the motion of the magnet-actuated autonomously-reciprocating in-cylinder regenerator and to test a graphite-glass clearance seal for piston scaling. Each of these purposes required different configurations of the engine simulator. As shown in Fig. 6.1, one configuration had a head that housed the regenerator mechanism and a piston-cylinder set with a magnet cap fixed to the top of the piston; and the other had a head that sealed the cylinder and provided a mount for a pressure transducer. For the second configuration, two different piston-cylinder sets were used for pressure testing. The simulator had a height from the base of the block to the top of the glass cylinder of 102 mm. Figure 6.2 shows a schematic of the simulator with the regenerator-mechanism head in place.

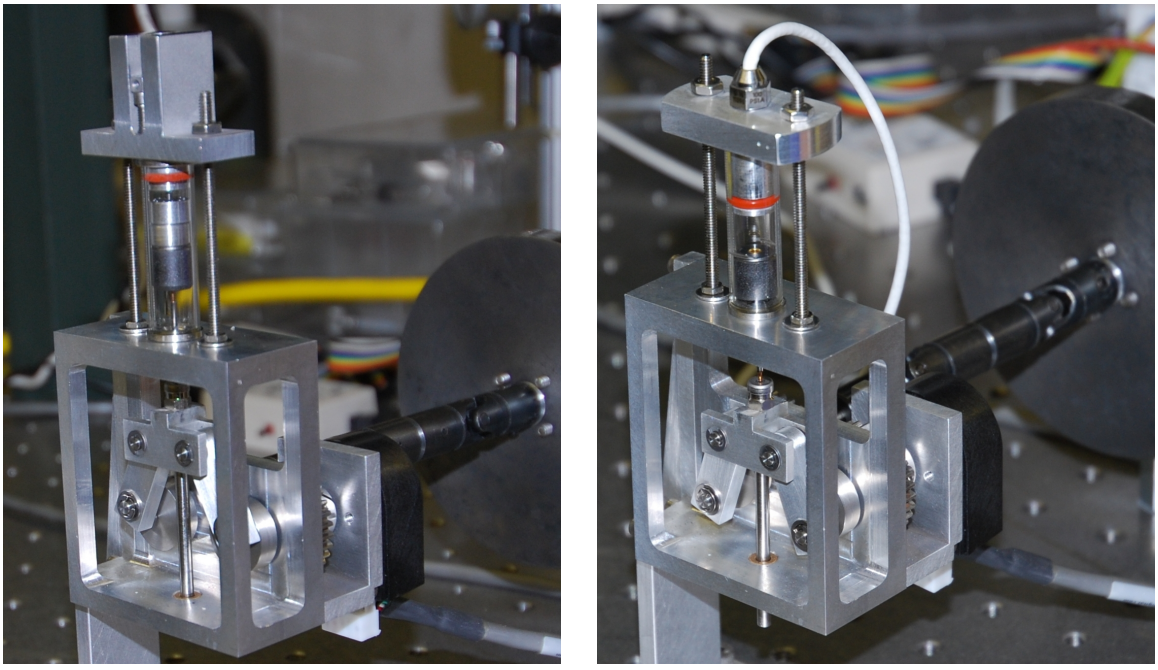

(a) The regenerator-mechanism head. (b) The pressure-testing head.

Figure 6.1: Photographs of the miniature atmospheric engine simulator with different heads in place.

There were several requirements for the simulator's design. Components requiring lubrication could not be used. In a real engine, the absence of lubrication could prevent fouling of the regenerator and catalytic ignition system. Moreover, the absence of a lubrication system leads to a simpler design. In addition, the drive mechanism could not impart a friction-causing side load, in the radial direction, on the piston. Lastly, the cylinder needed to be transparent. This requirement was necessary for inspecting the regenerator's motion with stop-motion photography.

The drive mechanism for the simulator was named the half-rhombic drive because of its similarity to the rhombic mechanisms found in beta Stirling engines. It was chosen because of its linear piston motion that, theoretically, imparts no radial loads on the piston. The drive mechanism was actuated by an input shaft that drove two drive gears connected to two connecting rods that reciprocated the yoke. It was sized by iteratively altering several parameters in its position function until the desired travel of 9.30 mm was reached; this was also the diameter of the piston. The kinematic equations of the half-rhombic mechanism, which include the position function, are presented in Appendix C.

All of the piston-cylinder sets used in the simulator were custom made by the Airpot Corporation and based upon their 2K95P actuator with a piston diameter of 9.30 mm. These unique components were made of graphite and borosilicate glass and had a lubrication-free low-friction clearance seal, where the average clearance between the piston and the glass was 4.45 μm. In addition, the glass cylinder was transparent and allowed for stop-motion photography of the regenerator's motion. The piston was connected to the yoke by the piston link with ball joints. Because of these ball-joints, the piston was unable to bear friction-causing moments.

The regenerator-mechanism head, which is shown with many important dimensions in Fig. 6.3, was designed with the assistance of the dynamic model. The regenerator's mass and dimensions were found using the dynamic model; this will be discussed later in Section 6.2. The regenerator mechanism was adjustable: the heights

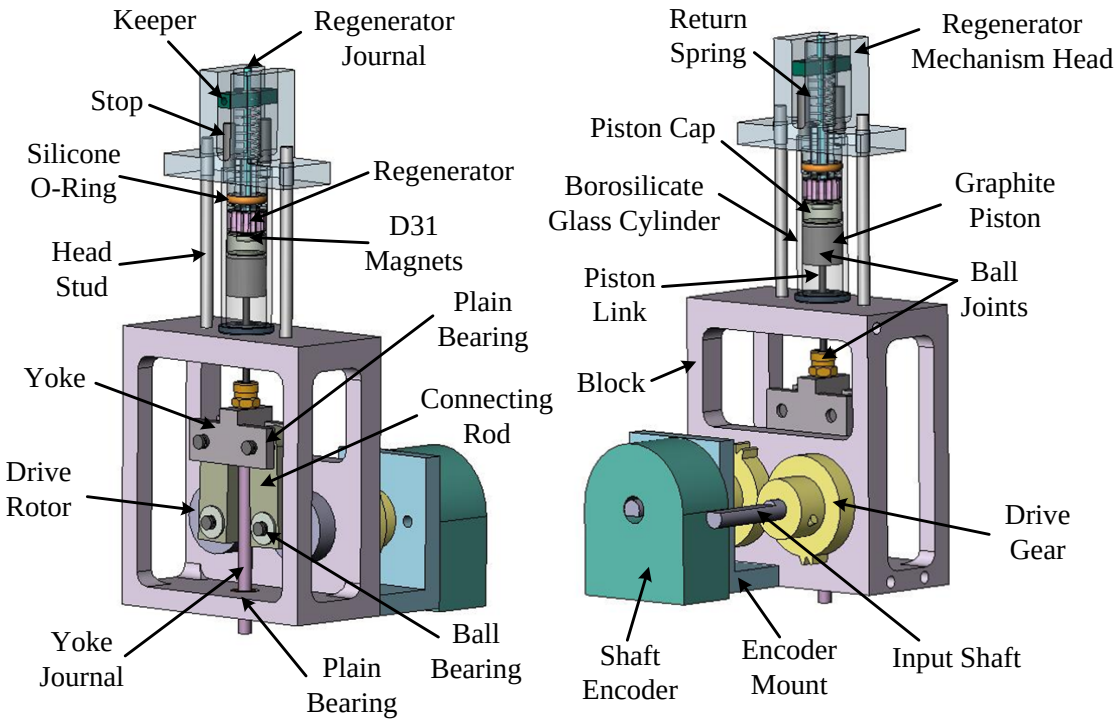

Figure 6.2: A schematic of the miniature atmospheric engine simulator.

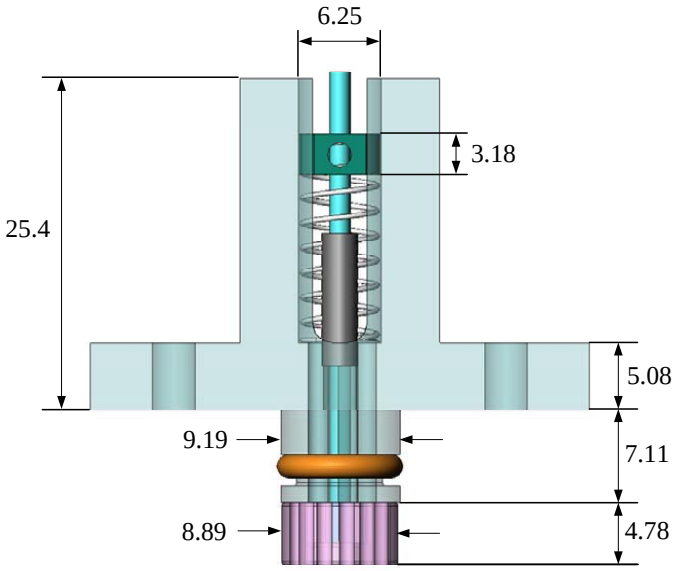

Figure 6.3: A schematic of the regenerator-mechanism head showing many important dimensions in mm.

of the keeper and the stop changed the regenerator travel and the rest-compression of the spring, and shims allowed adjustment of the separated piston-to-regenerator clearance at top dead center. The height of the keeper, which was clamped in place with a set screw, was adjusted by changing its location on the regenerator journal. The height of the stop, which was a stud threaded into the regenerator head, was changed by screwing it either in or out and fixing it in place with thread-locking compound. The regenerator journal, which connected the keeper and regenerator, passed through a bore in the head serving as a bearing. Ports located directly below the spring vented the top of the regenerator to atmospheric pressure at all times. The regenerator coupled to the magnet cap using two D31 magnets pressed into the magnet cap and the regenerator. The magnet cap was affixed to the piston using DP 105 epoxy made by 3M.

The pressure-testing head was simply an o-ring sealed plug that protruded into the cylinder. The clearance between the face of the plug and the piston at top dead center was set with shims. A pressure transducer was mounted in the top of the head, and it was vented to the cylinder by a port that was 1.5 mm in diameter and 13.1 mm in length.

6.2 Simulation of the Regenerator's Motion

Many elements of the miniature atmospheric engine simulator's design were based upon component availability; but the stiffness of the return spring and the mass and dimensions of the regenerator, all of which determined the regenerator's motion, were free parameters. They were examined by using the dynamic model, which was written in MATLAB, to simulate the regenerator's motion. The collection of programs for the dynamic model is presented in Appendix D.

A compression spring (Lee Spring model LC 016C 07 S) was selected for the engine simulator and had published values for stiffness and for free length of 30 N/m

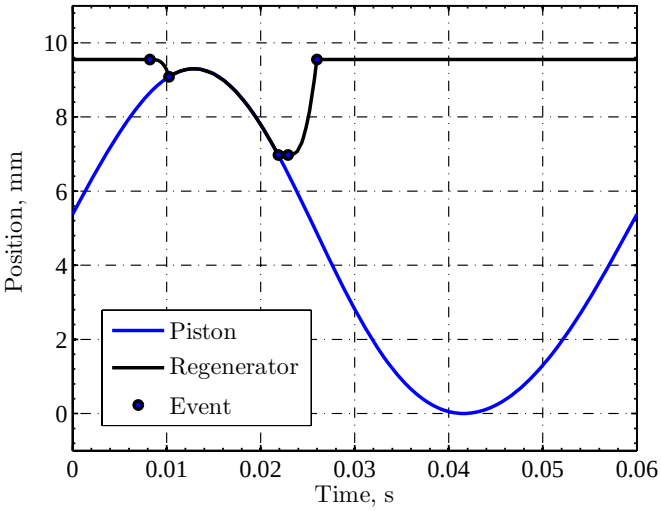

(a) An input shaft speed of 1000 rpm.

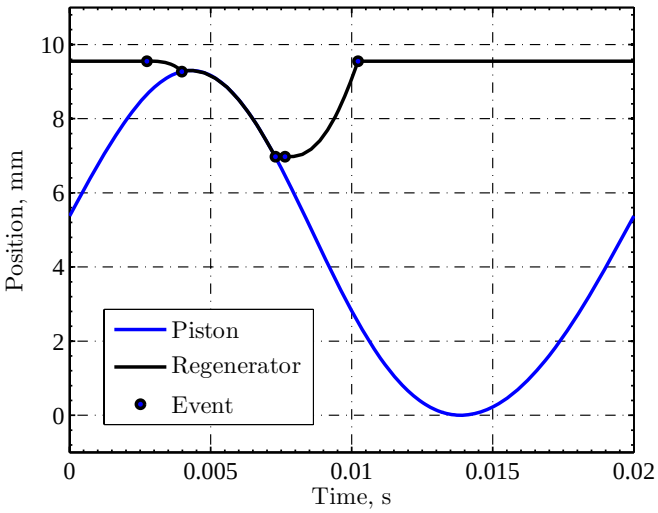

(b) An input shaft speed of 3000 rpm.

Figure 6.4: Simulations showing the position of the piston and regenerator as a function of time for two constant input shaft speeds.

and 17 mm, respectively. Simulations were performed using possible combinations of the regenerator's mass and dimensions. For these simulations, the spring's rest-compression with the regenerator at the top of the cylinder was 30 % of its free length; the separated piston-to-regenerator clearance with the piston at top dead center was 0.25 mm; and the regenerator's travel was restricted to 25 % of the piston's stroke. The kinematics of the piston were determined using the kinematic equations for the half-rhombic drive; these equations are presented in Appendix C. After examining many simulations, the following mass and dimensions were determined based upon a perception of the ideal regenerator motion inside the cylinder: $m = 1.81$ g, $H = 4.78$ mm, $p = 1.19$ mm, and $w = 0.20$ mm.

Figure 6.4 displays plots of simulations using the parameters described above. In the figure, the position of the regenerator and the piston are plotted as a function of time for constant input shaft speeds of 1000 rpm and 3000 rpm. At the higher input shaft speed, the piston and regenerator coupled later during the stroke of the piston. For both speeds, the piston and regenerator remained coupled until the keeper met the stop. The regenerator return times were 4 ms and 3 ms for input shaft speeds of 1000 rpm and 3000 rpm, respectively.

The uncertainty of the D31 magnet characterization was examined using simulations. The constants k_{Mag} and h_{Mag} were each changed by adding or subtracting one corresponding standard deviation (available from the two-magnet experiment) to create extreme functions for F_M. The data for the two-magnet experiment, including the uncertainty, was between these extreme functions. The model was then perturbed using the extreme functions and there were no significant effects.

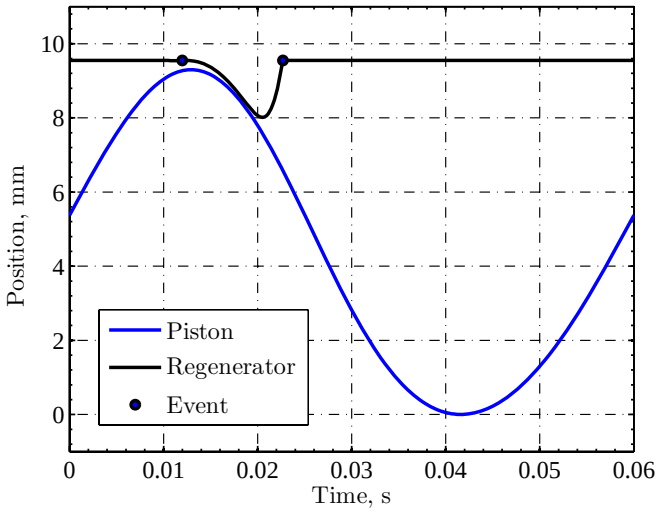

(a) $k_{Mag} = 3.15 \times 10^{-6}$ N/m.

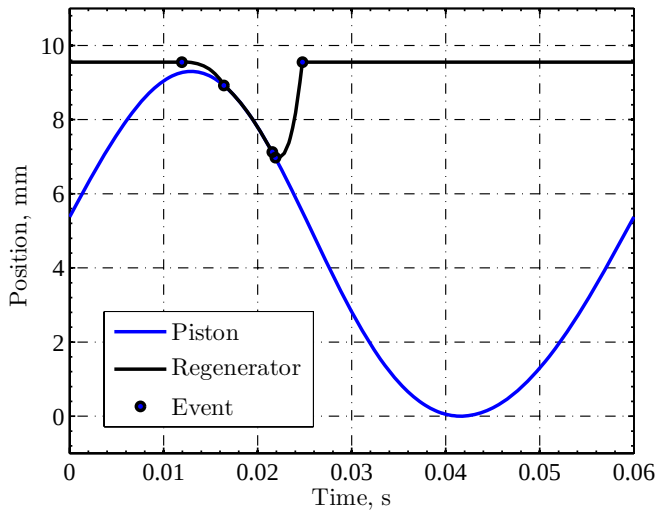

(b) $k_{Mag} = 3.19 \times 10^{-6}$ N/m.

Figure 6.5: Simulations using magnetic attraction force constants representing pairs of magnets with a weaker attraction force than a pair of D31 magnets. The shaft speed was constant at 1000 rpm.

Maximum Reynolds numbers of the fluid flowing the ports and through the clearance gap were calculated using the dynamic model. This was done to check the assumptions made in Section 4.3 that were part of the derivation for expressions accounting for the drag force and the pressure difference across the regenerator. The maximum Reynolds numbers were 560 and 190 for the regenerator ports and the clearance gap, respectively. Both numbers indicate laminar flow, which is consistent with the assumptions made.

Figure 6.5 displays plots of simulations using magnet constants representing pairs of magnets with a weaker attraction force than a pair of D31 magnets. For these simulations, k_{Mag} was either 3.15×10^{-6} N/m or 3.19×10^{-6} N/m; and the input shaft speed was constant at 1000 rpm. For both cases, the simulations for these weak attraction forces were undesirable. In (a) of Fig. 6.5, the regenerator and piston never coupled; and in (b), the regenerator and piston coupled only briefly. Premature ignition of the fuel-air charge during intake could occur in either case because of flow through the regenerator. The magnet constants used for these simulations are near a lower limit and are both approximately half of k_{Mag} for a pair of D31 magnets.

For a practical device, it would be desirable to design the magnets and the return spring to require as little power as possible. After all, the purpose of the regenerator is to boost efficiency. Power from the engine is required to separate the piston and the regenerator after they have decoupled. Choosing magnets with a minimal magnetic attraction force will reduce this loss. In addition, the spring requires power. When the piston is drawing the regenerator to the bottom of its travel, power is required to compress the spring. Choosing a spring with a minimal stiffness will reduce this loss. The engine simulator is the first prototype to incorporate a magnet-actuated regenerator. For future iterations, the knowledge learned from experimentation with this device can be used to optimize both the magnets and the spring. Moreover, if the concept proves to be commercially valuable, the magnets and the spring can be made to custom specifications.

7 Performance of the Reciprocating Regenerator

The engine simulator was used with a custom apparatus to examine the motion of the regenerator with stop-motion photography. The purpose of this experiment was to use experimental data to validate the dynamic model. In this chapter, the experimental methods used are explained; and the results are presented and discussed. For the results, data were superposed onto simulations using an algorithm. Overall, the data represented the simulations well. Thus, the dynamic model, though it is particular to a certain regenerator geometry, was validated.

7.1 Experimental Methods

The following sections describe the apparatus, procedures, and data reduction techniques used to examine the performance of the magnet-actuated autonomously-reciprocating in-cylinder regenerator.

7.1.1 Apparatus

The performance of the magnet-actuated autonomously-reciprocating in-cylinder regenerator was examined using stop-motion photography with a custom apparatus, which is displayed in Fig. 7.1. With the regenerator-mechanism head in place, the miniature atmospheric engine simulator was connected to a motor and a flywheel, which ensured regular motion of the half-rhombic drive and the regenerator mechanism. A motor control, which used feedback from the shaft encoder, powered the motor to maintain a constant speed. A digital single-lens-reflex camera, mounted on a tripod, was used to capture successions of stop-motion photographs while a strobe light, which created the illusion of slow motion, illuminated the engine simulator. A precision scale was fixed to the engine simulator so the positions of both the regenerator and the piston could be measured by examining the photographs. Several of the components used in this apparatus are described in Table 7.1.

7.1.2 Procedures

Four experiments were performed using two different springs and two different regenerator travels. In addition to the standard spring used to design the engine simulator (see Section 6.2), an alternate lower-stiffness spring (Lee Spring model LP 014B 03 S316) was used. The published values for its stiffness and free length were 90 N/m and 17 mm, respectively. This stiffness was 25 % of that of the standard

Table 7.1: Several of the components used to examine the motion of the autonomously-reciprocating regenerator.

Camera Body	
Manufacturer	Canon
Model Number	EOS Rebel XTi DS126151
Serial Number	0520135745
Camera Lens	
Manufacturer	Canon
Model Number	EFS 18–55 mm
Motor	
Manufacturer	Maxon
Model Number	144501
Serial Number	W02
Motor Control	
Manufacturer	Maxon
Model Number	4-Q-DC ADS 50/5 50V/5A
Serial Number	145391
Precision Scale	
Manufacturer	Starrett
Model Number	C303SR
Shaft Encoder	
Manufacturer	US Digital
Model Number	E2-512-250-HI-PKG2
Strobe Light	
Manufacturer	Omega
Model Number	HHT41

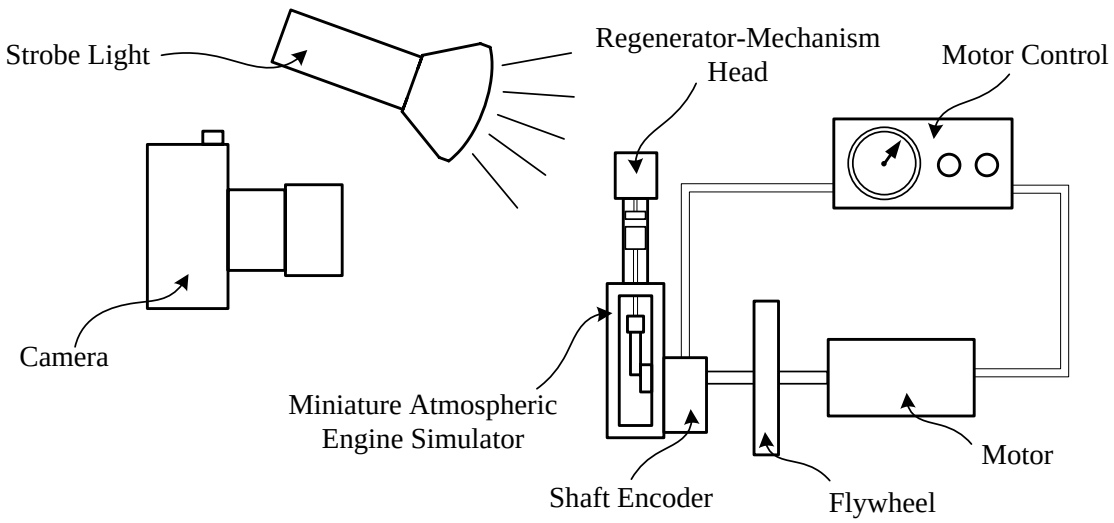

Figure 7.1: A schematic of the apparatus used to examine the motion of the autonomously-reciprocating regenerator.

spring. For both springs, regenerator travels of 20 % and 30 % of the piston's stroke were examined. For the four experiments, the rest-compression of each spring with the regenerator at the top of the cylinder was 30 % of its corresponding free length.

Data were gathered for the four experiments by inspecting stop-motion photographs. The engine simulator was operated at a constant input shaft speed of 1000 rpm and illuminated by the strobe light, which was cycled at 999 flashes per minute. The camera, set to a slow shutter speed of 17 ms, was used to capture successions of stop-motion photographs. A stop motion photograph, with the regenerator at the bottom of its travel, is shown in (a) of Fig. 7.2. The engine simulator was only operated for 1 min intervals; and between them, the regenerator was disassembled and thoroughly cleaned with isopropyl alcohol. This was done to prevent the accumulation of debris in the regenerator-mechanism head and to ensure consistent motion of the regenerator for all of the measurement intervals. Position measurements of both the piston and the regenerator were made by inspecting the stop-motion photographs of the engine simulator with the scale present; a sample photograph is shown in (b) of Fig. 7.2.

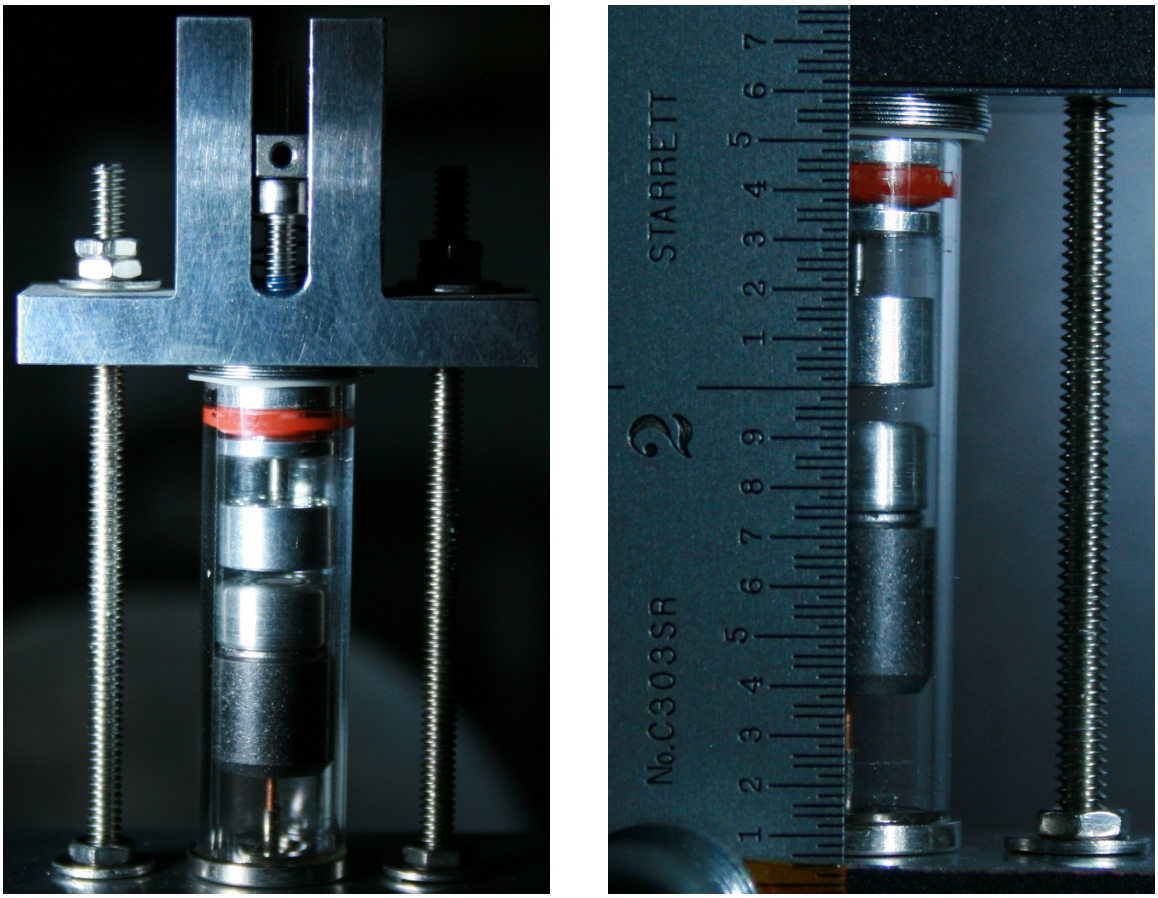

(a) The regenerator at the bottom of its travel.

(b) A photograph with the precision scale present for measurements.

Figure 7.2: Stop-motion photographs of the regenerator.

7.1.3 Data Reduction

The position data were superposed onto appropriate simulations using an algorithm that compared the data to the piston's kinematics and computed a vector comprised of times corresponding to the data points. The algorithm was written in MATLAB and is presented in Appendix E.

An uncertainty analysis was not performed for these experiments because the data were compared to simulations assumed to be perfect. However, if it is assumed the

algorithm has no uncertainty, then the uncertainty of the position of the regenerator is due only to the precision scale and can be approximated as ± 0.25 mm, which excludes precision error.

7.2 Results and Discussion

The experimental data and simulations for the four experiments are displayed in Fig. 7.3, where the windows of the plots include all interesting motion of the regenerator and are focused on the top half of the piston's stroke. In the experiments with the lower-stiffness spring, the regenerator lingered at the bottom of its travel for a considerable amount of time; this was probably due to the low spring stiffness. For all of the experiments, the data corresponding to the regenerator's movement back to the top of the cylinder lagged the simulation; this was probably due to sliding friction, a force that was not considered in the model. Also, the regenerator bounced when colliding with the top of the cylinder; in all cases, the height of the bounce was approximately 0.25 mm.

For the experiments involving the standard spring, the piston and regenerator coupled sooner than the model predicted. It is likely this early coupling was due to an actual spring stiffness less than that published. These standard-spring experiments, represented by (a) and (c) in Fig. 7.3, showed the motion of the regenerator can closely resemble the ideal operation: the regenerator and piston coupled before the piston reached top dead center; the regenerator quickly returned to the top dwell phase. Overall, the simulations were represented well by the experimental data. For this reason, the dynamic model, though it is particular to a certain regenerator geometry, was validated.

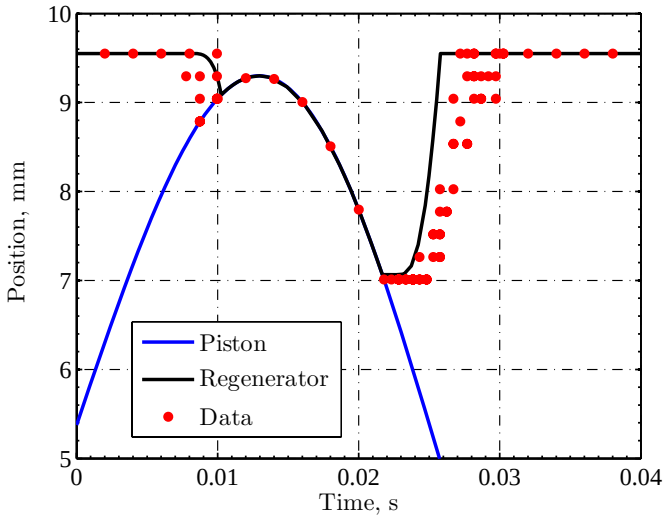

(a) 20 % of the piston's stroke with the standard spring.

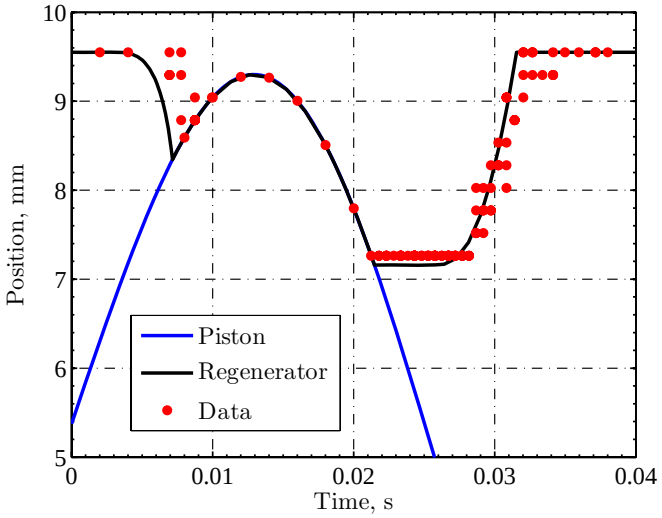

(b) 20 % of piston's stroke with the lower-stiffness spring.

Figure 7.3: Plots of the experimental data superposed onto appropriate simulations for the four experiments, which were completed with the atmospheric engine simulator operating at a constant input shaft speed of 1000 rpm. The windows of the plots include all interesting motion of the regenerator and are focused on the top half of the piston's stroke.

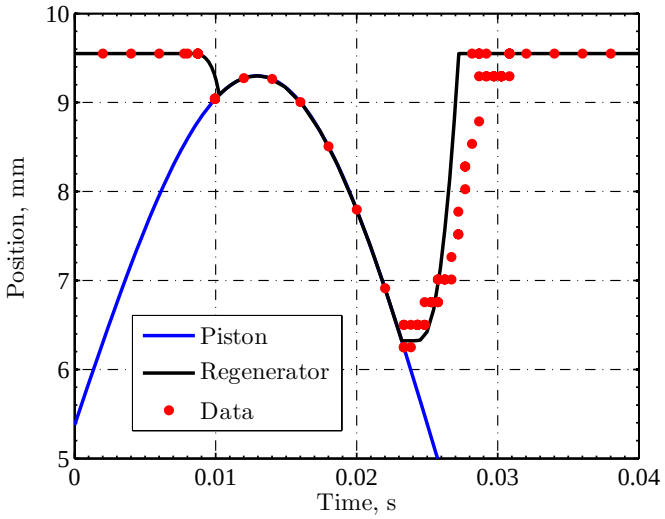

(c) 30 % of piston's stroke with the standard spring.

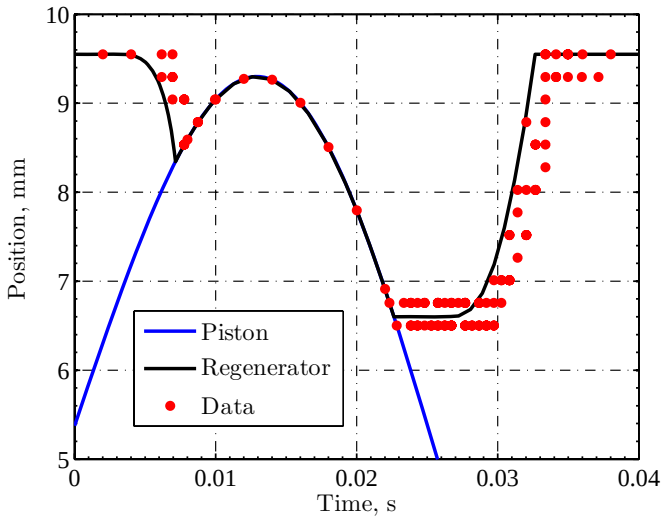

(d) 30 % of piston's stroke with the lower-stiffness spring.

Figure 7.3: Plots of the experimental data superposed onto appropriate simulations for the four experiments, which were completed with the atmospheric engine simulator operating at a constant input shaft speed of 1000 rpm. The windows of the plots include all interesting motion of the regenerator and are focused on the top half of the piston's stroke.

8 Performance of the Graphite-Glass Clearance Seal

The engine simulator was used with a custom apparatus to test the performance of the graphite-glass clearance seal. The experiments performed had two purposes: to gain knowledge for future piston scaling studies and to examine the longevity of the graphite-glass clearance seal. In this chapter, the experimental methods used are explained; and the results are presented and discussed. It was found that the leak effect of the graphite-glass seal was less considerable at higher cycle speeds. It was also found that over a 26 h period of operation the graphite piston did not show considerable wear. However, the ball joints supporting the piston became worn and were responsible for a trend indicating reduced peak cycle pressure with time.

8.1 Experimental Methods

The following sections describe the apparatus, procedures, and data reduction techniques used for pressure experiments that involved two different types of piston-cylinder sets.

8.1.1 Apparatus

The performance of the graphite-glass clearance seal was tested with a custom apparatus, which is displayed in Fig. 8.1. The apparatus used for these experiments was nearly the same as that used for examining the performance of the autonomously-reciprocating regenerator. Therefore, information regarding the motor, the motor control, and the shaft encoder can be found in Table 7.1. For these experiments, the miniature atmospheric engine simulator was was configured for pressure tests, which required the pressure-testing head and the use of one of two different types of piston-cylinder sets. A data acquisition chassis served as an interface between a computer and both the shaft encoder and the pressure transducer, which was mounted in the pressure-testing head. Several of the components used for the pressure experiments are described in Table 8.1.

Two different types of Airpot Corporation piston-cylinder sets were required for the pressure experiments. One set was plain, and the other was slotted. The slotted piston-cylinder set was made by cutting two identical slots on opposite sides of the glass cylinder situated just above bottom dead center of the piston. The slots were cut using a precision saw with a blade having a thickness of 0.53 mm (Buehler IsoMet 1000). Figure 8.2 shows a schematic of the slotted piston-cylinder set. The slots, which had dimensions 0.53 mm $\times$ 3.0 mm, served to equalize the cylinder pressure with atmospheric pressure during the bottom of each piston stroke.

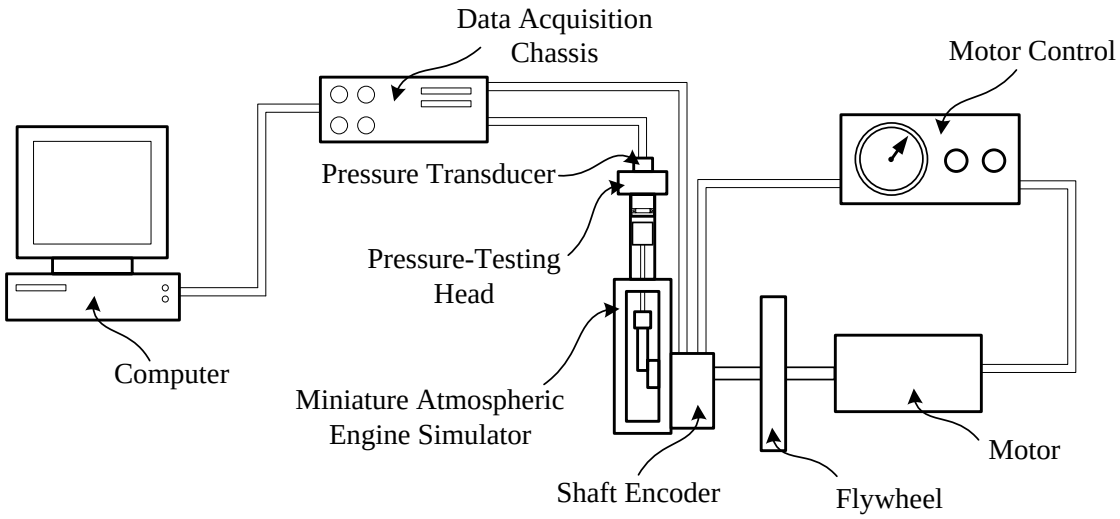

Figure 8.1: A schematic of the apparatus used to test the performance of the graphite-glass clearance seal.

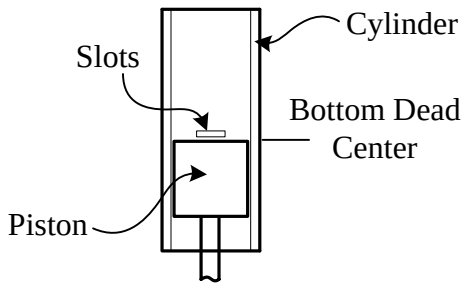

Figure 8.2: A schematic of the slotted piston-cylinder set.

Table 8.1: Several of the components used to test the performance of the graphite-glass clearance seal.

Computer	
Manufacturer	Dell
Model Number	Optiplex
Serial Number	F83SS01
Data Acquisition Chassis	
Manufacturer	Omega
Model Number	OM5-BP-16-C
Serial Number	253111 0406
Encoder Digital to Analog Converter	
Manufacturer	US Digital
Model Number	EDAC
Pressure Gauge for Atmospheric Pressure	
Manufacturer	Oakton
Model Number	WD-03316-80
Serial Number	04960
Uncertainty	$u_{PAtm} = 0.339$ kPa
Pressure Gauge for Calibration	
Manufacturer	Dwyer
Model Number	7214D-G100
Serial Number	N49L
Uncertainty	$u_{PC} = 1.723$ kPa
Pressure Transducer	
Manufacturer	Endevco
Model Number	8530C-100
Serial Number	11396
Notes	Combined Error = 0.4 % of Full Scale Output, Excitation = 10 V, Rated Output = 2.25 mV/psi
Uncertainty	$u_{PT} = 0.9 \times 10^{-3}$ V
Signal Conditioning Module for Pressure Transducer	
Manufacturer	Omega
Model Number	OM5WV-1A-C
Serial Number	7733-11 0403
Signal Conditioning Module for Shaft Encoder	
Manufacturer	Omega
Model Number	OM5WV-1A-C
Serial Number	8277-47 0408

8.1.2 Procedures

Two types of experiments were completed to test the performance of the graphite-glass clearance seal. For the first type of experiment, pressure data were acquired for many constant speeds using both the plain cylinder and the slotted cylinder. For the second type of experiment, which was a long-duration test, the engine simulator was operated with the slotted piston-cylinder set at one constant speed; and pressure data were gathered at regular intervals. For all of the experiments, the face of the pressure testing head was located 0.25 mm above the top face of the piston while at top dead center.

Before completing any series of measurements, both the pressure transducer and the shaft encoder were calibrated. A two-point calibration, similar to that used for the magnet tests, was used to calibrate the pressure transducer. The pressure-testing head with the pressure transducer in place was either connected to a high pressure source and a pressure gauge for calibration or vented to atmospheric pressure. The high pressure source supplied a pressure of 400 kPa, which was higher than the maximum pressure expected during the experiments. For both of the calibration pressures, the pressure transducer voltages were recorded by LabVIEW. These measurements were then used to complete the two-point calibration, which was a linear function relating pressure to the pressure transducer output voltage.

The shaft encoder was calibrated so it's zero occurred when the piston was at bottom dead center. This calibration was accomplished by first recording the encoder's output voltage while the piston was at bottom dead center. Then, this voltage and the encoder's maximum output voltage were manipulated using the modulo function to set the encoder's zero at bottom dead center of the piston in the LabVIEW program.

For both the plain and slotted piston-cylinder sets, pressure data were acquired for many constant engine simulator speeds. Before gathering any data, both the pressure transducer and the shaft encoder were calibrated. Then, data were recorded using LabVIEW with the engine simulator set to a constant input shaft speed between 200 rpm and 1800 rpm in increments of 400 rpm. The sampling frequency of the LabVIEW program was changed for each engine simulator speed so that about 720 data points were collected for each pressure data set.

Long-duration pressure experiments were performed using the engine simulator operating at 1400 rpm with the slotted piston-cylinder set. Two types of long duration experiments were performed. For one experiment, the duration was 24 hr; and data were collected every hour. For the other, the duration was 120 min; and data were collected every 10 min. For both experiments, the measurement intervals were timed using a stopwatch. The pressure transducer and the shaft encoder were calibrated before starting each experiment. Atmospheric pressure was monitored during both of the experiments; and when it changed by 0.339 kPa, which was one increment of the pressure gauge used for measuring atmospheric pressure, the pressure transducer was again calibrated. Data were recorded using LabVIEW; and for any given measurement, data were collected seven times so precision error could be considered. Between each of the measurements at the same engine simulator speed, the engine simulator speed was reset; this was done to properly account for precision error.

8.1.3 Data Reduction

A computer with LabVIEW was used to record data for all of the pressure experiments. The LabVIEW program recorded pressure data sets from the experiment during operation and used the periodic sawtooth-shaped encoder signal to decide when to start and stop the acquisition of a curve. For every pressure data set, a data file was recorded; and from them, some of the following plots were created for

each experiment: P-V, pressure ratio versus engine simulator speed, pressure ratio with respect to atmospheric pressure versus engine simulator speed, maximum pressure versus time, and minimum pressure versus time. For both the maximum pressure versus time and minimum pressure versus time plots for the long-duration experiments, the data points were an average of seven measurements.

Uncertainty analyses were performed for all plots excluding the P-V curves using the Kline-McClintock method [57]. The uncertainty analyses accounted for bias error; and for the long-duration experiments, they also accounted for precision error. The uncertainty analyses are presented in Appendix F.

8.2 Results and Discussion

Following, the results from the pressure experiments that involved different constant input shaft speeds are presented and discussed. Figure 8.3 displays plots for the plain piston-cylinder pressure experiment that involved different constant input shaft speeds. As shown in (a) of Fig. 8.3, which is a family of P-V curves, there was a partial vacuum for about half of the cycle for all of the speeds. For all of the P-V curves from the pressure experiments, there is a gap in the expansion stroke data due to the triggering of the LabVIEW program. For all of the P-V curves, the maximum pressures were approximately 185 kPa; and the minimum pressures were between approximately 40 kPa and approximately 50 kPa. Increased input shaft speeds yielded a lower minimum pressure and a steeper overall P-V curve. It is important to note that the expansion and compression processes did not intersect for any speed. However, their difference was less for higher input shaft speeds. As shown in (b) of Fig. 8.3, the pressure ratio increased with increased input shaft speed from approximately 4.1 to approximately 5.

Figure 8.5 displays plots for the slotted piston-cylinder pressure experiment involving different constant input shaft speeds. As shown in (a) of Fig. 8.5, which is a family of P-V curves, during the expansion stroke of the cycle a partial vacuum was drawn. Then, when the slots were exposed by the piston, the pressure within the cylinder equalized with atmospheric pressure. For the input shaft speeds tested, the maximum pressure was approximately 370 kPa, and the minimum pressure was approximately 70 kPa. The magnitude of the partial vacuum drawn decreased with increased input shaft speed for all of the P-V curves. Also, the P-V curves became more steep with increased input shaft speed. As with the experiment involving the plain piston-cylinder set, the expansion and compression processes never intersected. Their difference decreased with increased input shaft speed. From (b) and (c) of Fig. 8.5, which are separate plots of pressure ratio versus input shaft speed and pressure ratio with respect to atmospheric pressure versus input shaft speed, it can be seen that both increased with increased input shaft speed. In the case of the pressure ratio, it increased from approximately 3.75 to approximately 4.2. And, in the case of the pressure ratio with respect to atmospheric pressure, it increased from approximately 2.6 to approximately 3.6. The pressure behavior for this experiment was different than that of the plain piston-cylinder set. The maximum pressure was considerably higher, and the expansion and compression processes, as shown in the P-V curves are more dissimilar.

It is necessary to discuss the heat transfer during compression and expansion processes for conditions similar to that of these experiments. During the compression process, a temperature gradient is established due the increased energy of the working fluid. As a result, heat is transferred to the cylinder wall. During the expansion process, the energy of the working fluid is then reduced. After subsequent compression-expansion cycles, heat is transferred to the surroundings; and this heat-transfer effect can cause a lower overall temperature and pressure of the working fluid.

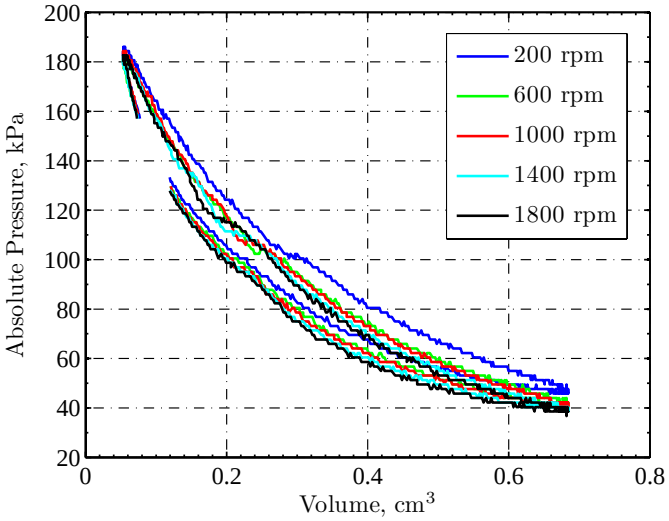

(a) Absolute pressure versus volume (P-V).

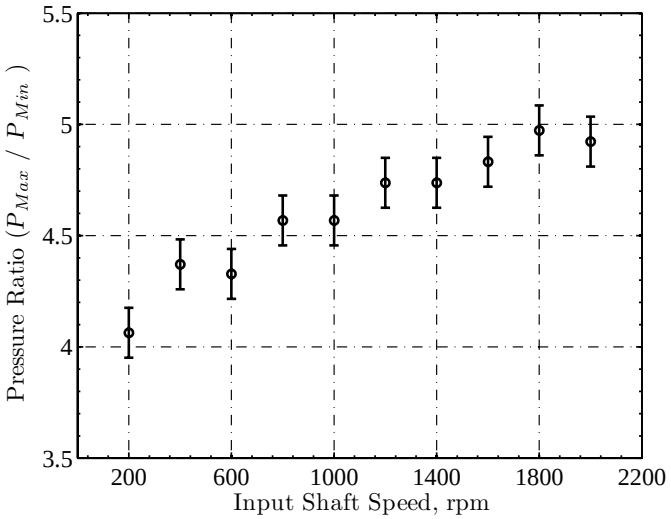

(b) Pressure ratio versus input shaft speed.

Figure 8.3: Plots for the plain piston-cylinder pressure experiment involving different constant input shaft speeds.

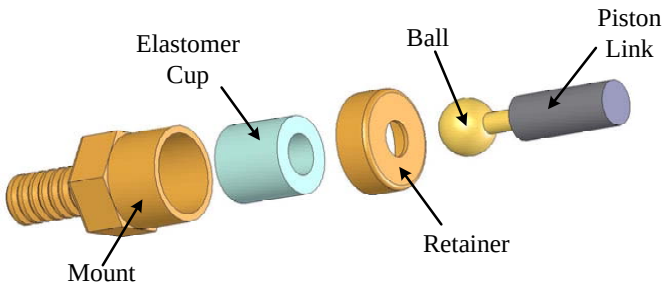

Figure 8.4: A schematic of the ball joint made by the Airpot Corporation.

In the case of these experiments, the expansion and compression processes did not intersect, and this indicates external work was required for the thermodynamic cycle. This effect was more noticeable for the experiment involving the slotted piston-cylinder. After careful observation of the engine simulator while in motion, small elastic deflections of the piston at top and bottom dead center were noticed. With further inspection, it was found that the ball joints were deflecting. A schematic of an Airpot Corporation ball joint is shown in Fig. 8.4. The elastomer cup, which is a part contained in the ball joint, deflected during the cycle. For the experiment involving the slotted piston-cylinder set, additional mass was transferred during the cycle beyond that due to leakage alone. This increased mass transfer was due to the slots. The deflection of the ball joints; the leakage due to the clearance seal or the leakage due to the clearance seal and the mass transfer due to the slots; and the aforementioned heat-transfer effect should account for the apparent work required for the thermodynamic cycle, which was more for the slotted piston-cylinder.

Two conclusions can be made from the trends in the plots shown in Fig. 8.3 and Fig. 8.5. First, the leakage effect of the clearance seal becomes less at higher input shaft speeds. This was expected because there is less time for working fluid to escape or enter the cylinder. Second, as indicated by the increased steepness of the P-V curves, the expansion and compression processes behave in a more adiabatic manner at higher input shaft speeds; this was expected because there is less time

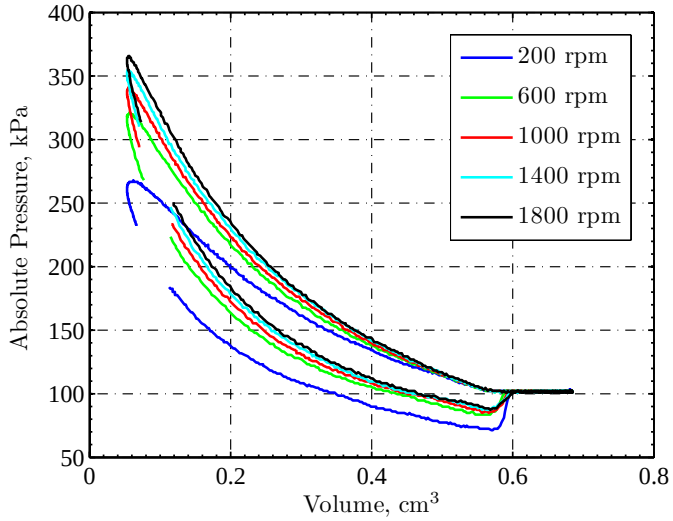

(a) Absolute pressure versus volume (P-V).

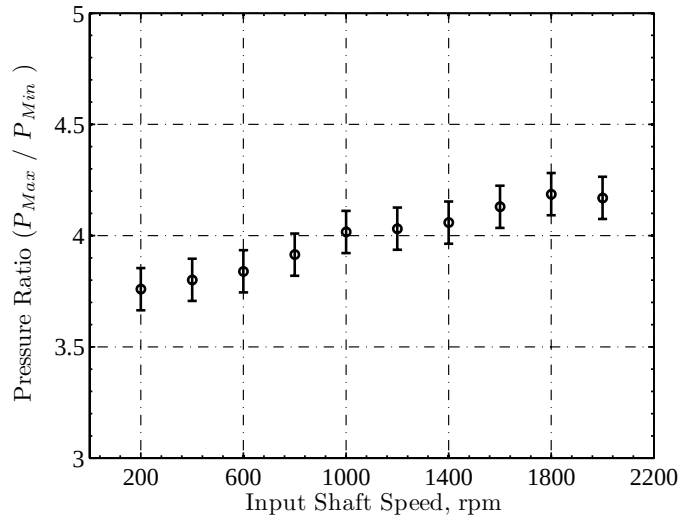

(b) Pressure ratio input shaft speed.

Figure 8.5: Plots for the slotted piston-cylinder pressure experiment involving different constant input shaft speeds.

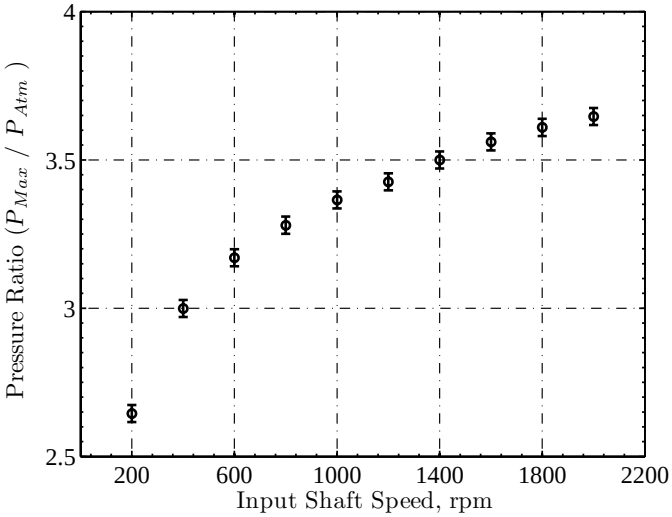

(c) Pressure ratio with respect to atmospheric pressure versus input shaft speed.

Figure 8.5: Plots for the slotted piston-cylinder pressure experiment involving different constant input shaft speeds.

for heat transfer processes to occur in the cycle. The concerted effects of both the heat transfer from the compressed working fluid and the leakage from the cylinder are difficult to separate. Therefore, quantifying the influence from each effect on the cycle's behavior is intractable. The Airpot Corporation, however, has published the leakage rates for the 2K95P actuator, which uses a similar piston-cylinder set as those used for these experiments. The leakage rates are 0.36 L/min and 1.17 L/min for pressures of 344 kPa and 689 kPa, respectively. These rates are normalized to air at atmospheric pressure and room temperature.

Following, the results for the long-duration pressure experiments are presented and discussed. Figure 8.6 displays the results for the long-duration 24 hr pressure experiment with the engine simulator operating at 1400 rpm. As shown in (a) of Fig. 8.6, which is a plot of maximum absolute pressure versus time, the maximum pressure decreased from approximately 364 kPa to approximately 340 kPa during the duration of the test. From (b) of Fig. 8.7, which is a plot of minimum absolute

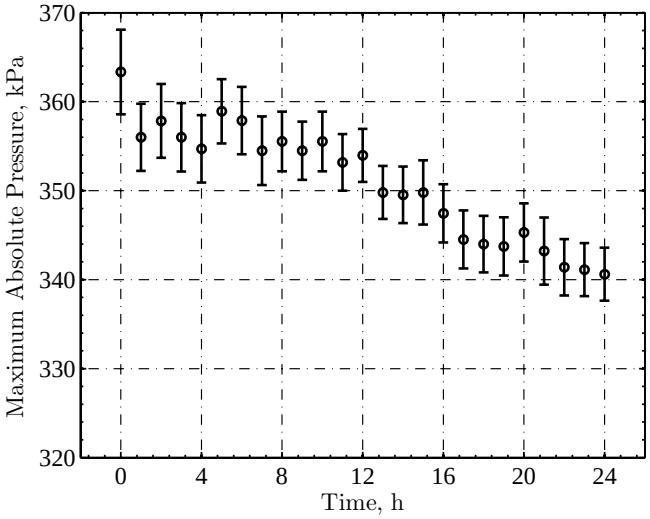

(a) Maximum absolute pressure as a function of time.

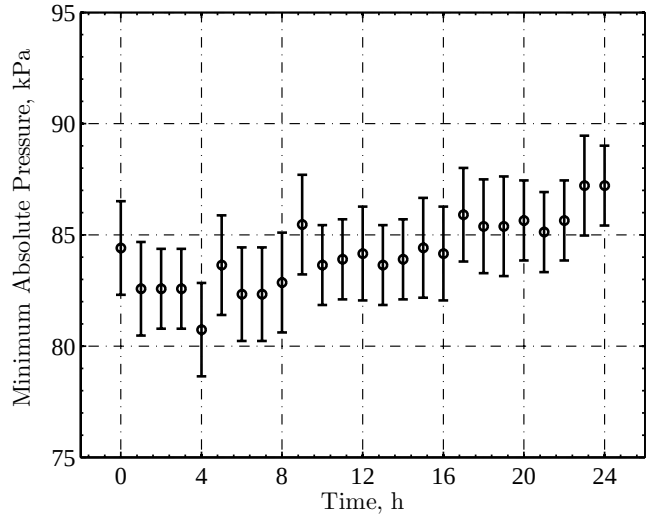

(b) Minimum absolute pressure as a function of time.

Figure 8.6: Plots for the long-duration 24 h pressure experiment with the engine simulator operating at 1400 rpm.

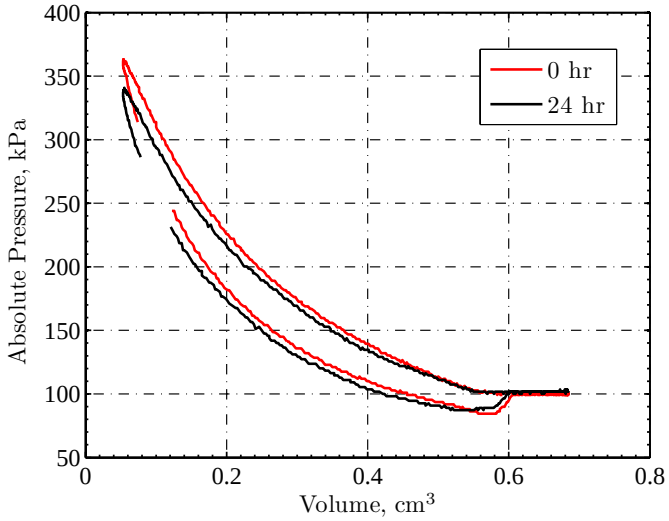

(c) Absolute pressure versus volume (P-V).

Figure 8.6: Plots for the long-duration 24 h pressure experiment with the engine simulator operating at 1400 rpm.

pressure versus time, the minimum pressure increased from approximately 83 kPa to approximately 87 kPa. And, in (c) of Fig. 8.6, which shows P-V curves, the difference between the shapes of the P-V curves can be seen. During the test, no significant wear of the half-rhombic drive was noted.

The long-duration experiment was continued for another 2 h with a finer resolution of 10 min. The results from this test are shown in Fig. 8.7. It must be noted that the first data points of the pressure plots do not match the endpoints from the previous long-duration test. This discrepancy is due to uncertainty in the calibration process. From the plots in Fig. 8.7, notice that the maximum pressure decreased from approximately 336 kPa to approximately 332 kPa with time. Again, there was no significant wear of the piston-cylinder set.

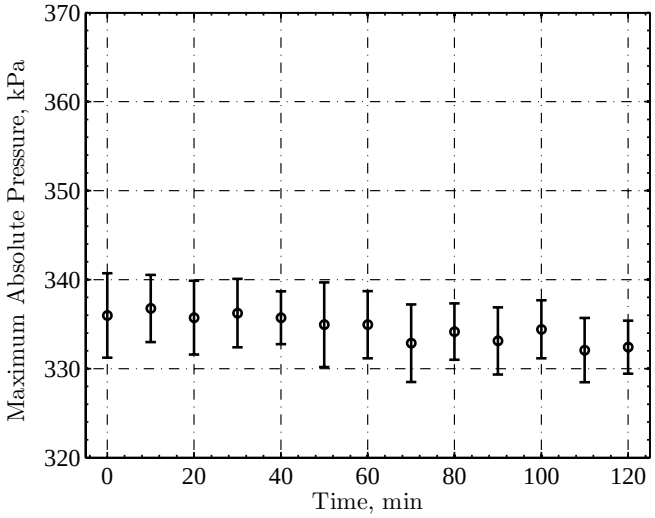

(a) Maximum absolute pressure as a function of time.

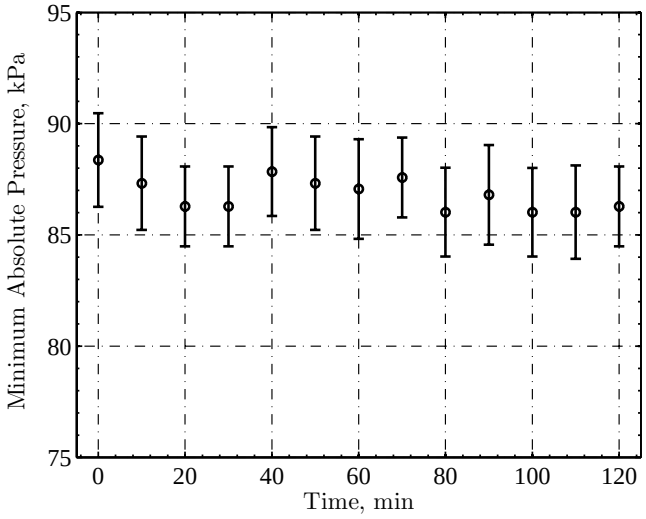

(b) Minimum absolute pressure as a function of time.

Figure 8.7: Plots for the long-duration 120 min pressure experiment with the engine simulator operating at 1400 rpm.

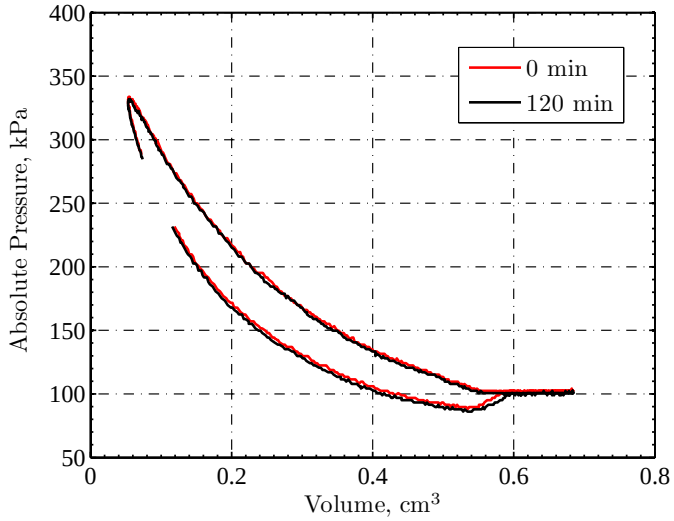

(c) Absolute pressure versus volume (P-V).

Figure 8.7: Plots for the long-duration 120 min pressure experiment with the engine simulator operating at 1400 rpm.

From the plots in Fig. 8.6 and Fig. 8.7, one trend can be inferred. The maximum pressure decreased with time. After these experiments, the slotted piston-cylinder set was carefully examined. No apparent wear of the piston was noted. This was expected: according to the Airpot Corporation, the piston-cylinder set should withstand millions of cycles, and the set used in the experiment was cycled about 2.2 million times. However, at the end of the experiment, the ball joints had considerable play when compared to an unused piston cylinder set. It is likely the decrease in pressure is due to the wear in the elastomer cups in the ball joints (Fig. 8.4) and not due to deterioration of the graphite-glass clearance seal.

9 Conclusions

Many firms are researching small-scale engines for portable power applications to utilize the high energy density of liquid hydrocarbon fuels. The concepts for these engines range from familiar designs adapted to the small scale to specifically developed novel designs. With all of these efforts, however, no successful small-scale engine has been created. In other words, several small-scale engines have been demonstrated to operate; but, at best, their efficiencies have been poor.

One possible alternative for improving the efficiency of small-scale heat engines is the incorporation of thermal regeneration, which is the beneficial use of heat energy that has been produced within an engine's thermodynamic cycle. It has been shown with thermodynamics that the regenerated atmospheric power cycle, with the usual air-standard assumptions, is exceptionally sensitive to regeneration. For this reason, a concept for a miniature atmospheric engine with a magnet-actuated autonomously-reciprocating in-cylinder regenerator has been developed.

As part of the development of the proposed engine, a dynamic model of the regenerator's motion was created and a miniature atmospheric engine simulator was designed and fabricated. The dynamic model was created for two purposes. First, it was necessary for completion of the engine simulator. Second, knowledge of the regenerator's motion, which is provided by the dynamic model, is necessary for the development of a thermal model. The engine simulator was used to examine the motion of the regenerator with stop-motion photography. It was demonstrated that the regenerator's motion closely resembled the ideal concept of operation. Furthermore, data from the stop-motion photographs were used to validate the dynamic model.

Simplicity was central to the concept development of the proposed engine; and to this effect, an effort was made to incorporate lubrication-free components. The most notable among these components was a unique graphite-glass piston-cylinder set with a lubrication-free clearance seal. Experiments were performed with two versions of

this unique component as a first step to determine whether it would be appropriate for practical use. Pressure data over a range of operation speeds were gathered for slotted and plain versions of the piston cylinder set. The maximum pressure ratio for the plain set was approximately 5, which was larger than the maximum pressure ratio of approximately 4.2 for the slotted set. In contrast, the maximum pressure of approximately 370 kPa for the slotted set was greater than the maximum pressure of approximately 185 kPa for the plain piston-cylinder set. P-V curves were also gathered for both piston-cylinder sets, and they became steeper with increased operation speed.

From these data, it can be concluded that the slotted piston-cylinder set yielded a higher peak pressure and lower overall pressure difference than the plain piston-cylinder set. In addition, the leakage effect of the clearance seal lessens at higher input shaft speeds. Also, as indicated by the increased steepness of the P-V curves, the expansion and compression processes behave in a more adiabatic manner at higher operation speeds.

For the slotted piston-cylinder set, pressure data at a constant operation speed was gathered over a 26 h period. The maximum pressure decreased with time. It was determined, with careful inspection, that the graphite-glass seal was not the reason for this fall in pressure. Instead, this fall in pressure was due to the wear of the elastomer cups that are part of the ball joints supporting the graphite piston. Over this 26 h period, no noticeable wear of the half-rhombic drive was noted. Moreover, even with the presence of the slots, the graphite piston also did not show any significant wear.

Further work is necessary to determine the feasibilities of the use of both the magnet-actuated autonomously-reciprocating in-cylinder regenerator and the graphite-glass piston-cylinder set. Now that the dynamic model has been created, future work should include development of a thermal model, which would use the dynamic model, to inspect this particular implementation of regeneration. As part of this modeling effort, the dynamic model should be modified to handle an experimentally found friction-factor for a practical regenerator and to account for forces caused by combustion. It has been shown that the graphite-glass piston cylinder set can withstand long-duration use. However, the tests were performed at room temperature. Future work should also include hot testing of the graphite-glass piston cylinder set.

References

[1] T. Herron, H. Wang, and R. B. Peterson. Performance of a reciprocating expander-compressor for a miniature heat-actuated heat pump. In *Proceedings of the 3rd International Energy Conversion Engineering Conferene and Exhibit*, 2005.

[2] R. B. Peterson. A scaling study of a combined microcombustor and heat engine system. *Journal of Power and Energy—Part A*, 219:371–381, 2005.

[3] K. D. Annen, D. B. Stickler, and J. Woodroffe. Glow plug-assisted HCCI combustion in a miniature internal combustion engine (MICE) generator. In *Proceedings of the 44th AIAA Aerospace Sciences Meeting and Exhibit*, 2006, AIAA 2006-1349.

[4] K. D. Annen, D. B. Stickler, and J. Woodroffe. Miniature internal combustion engine (MICE) for portable electric power. In *Proceedings of the 23rd Army Science Conference*, 2002.

[5] A. H. Epstein, S. A. Jacobson, J. M. Protz, and L. G. Frechette. Shirtbutton-sized gas turbines: The engineering challenges of micro high speed rotating machinery. In *8th International Symposium on Transport Phenomena and Dynamics of Rotating Machinery*, 2000.

[6] S. P. Dev. Quiet, small, light-weight, heavy-fueled mini generator sets for power needs of soldiers and unmanned ground vehicles. In *Proceedings of the 23rd Army Science Conference*, 2002.

[7] W. J. A. Dahm, J. Ni, K. Mijit, J. R. Mayor, G. Qiao, and S. W. Dyer. Micro internal combustion swing engine (MICSE) for portable power generation systems. In *Proceedings of the 40th AIAA Aerospace Sciences Meeting*, 2002, AIAA 2002-0722.

[8] S. Stephens. The incredible shrinking engine. *Forefront*, pages 10–13, 2001.

[9] D. Dunn-Rankin, E. M. Leal, and D. C. Walther. Personal power systems. *Progress in Energy and Combustion Science*, 31:422–465, 2005.

[10] C. H. Lee, K. C. Jiang, P. Jin, and P. D. Prewett. Design and fabrication of a micro wankel engine using MEMS technology. *Microelectronic Engineering*, 73–74:529–534, 2004.

[11] A. H. Epstein, S. D. Senturia, I. A. Waitz, and J. H. Lang. Microturbomachinery. United States Patent No. 5,932,940, 1999.

[12] F. Hapgood. Peewee power. *Smithsonian*, pages 36–37, 2002.

[13] J. Peirs, D. Reynaerts, and F. Verplaetsen. Development of an axial microturbine fo a portable gas turbine generator. *Journal of Micromechanics and Microengineering*, 13:S190–S195, 2003.

[14] D. Wiberg, S. Vargo, V. White, and K. Shcheglov. Miniature gas-turbine power generator. *NASA Technical Briefs*, 2003.

[15] K. Isomura, M. Murayama, S. Teramoto, K. Hikichi, and Y. Endo. Experimental verification of the feasibility of a 100 W class micro-scale gas turbine at an impeller diameter of 10 mm. *Journal of Micromechanics and Microengineering*, 16:S254–S261, 2006.

[16] K. D. Annen, D. B. Stickler, and P. L. Kebabian. Miniature generator. United States Patent No. 6,349,683, 2002.

[17] D. V. Green, C. G. Miller, D. A. Santavicca, and K. V. Sharp. Pulsed micro catalytic combustor for use in a solid piston microengine. In *Proceedings of the ASME International Mechanical Engineering Congress and Exposition*, 2004, IMECE2004-61644.

[18] I. Urieli and D. M. Berchowitz. *Stirling Cycle Engine Analysis*. Adam Hilger, 1984.

[19] P. P. Walsh and P. Fletcher. *Gas Turbine Performance*. Blackwell Science, 2004.

[20] G. Walker. *Stirling Engines*. Clarendon Press, 1980.

[21] A. J. Organ. Regenerator thermal design in a nutshell. In *Proceedings of the Institution of Mechanical Engineers*, 2000.

[22] A. J. Organ. *The Regenerator and the Stirling Engine*. J. W. Arrowsmith, 1997.

[23] W. M. Kays and A. L. London. *Compact Heat Exchangers*. Krieger Publishing Company, 1984.

[24] K. Pattas. Thermal engine, especially piston engine. United States Patent No. 3,777,718, 1973.

[25] M. W. Millman. Regenerative reciprocating open cycle internal combustion engine. United States Patent No. 4,280,468, 1981.

[26] E. L. Keating and A. A. Pouring. Internal regenerative air standard internal combustion engine cycle performance. In *Proceedings of the 18th Joint Propulsion Conference*, 1982.

[27] E. L. Keating, A. A. Pouring, and R. Chute. Internally regenerative engine cycle analysis: A parametric study. In *Proceedings of the ASME Winter Annual Meeting*, 1983.

[28] N. Isshiki, B. Wen, M. Isshiki, and T. Torizuka. Performance of internal combustion Stirling engine. In *Proceedings of the 2nd International Conference on Stirling Engines*, 1984.

[29] S. Moriya, N. Isshiki, and S. Kikuchi. Studies on regenerator element for internal combustion Stirling engine. In *Proceedings of the 5th International Stirling Engine Conference*, pages 291–296, 1991.

[30] S. Moriya and N. Isshiki. Regenerator elements for internal combustion Stirling engine. In *Proceedings of the 27th Intersociety Energy Conversion Engineering Conference*, volume 5, pages 405–410, 1992.

[31] R. Pavletič, B. Vuksanović, and A. Pečjak. Regeneration of heat in piston internal combustion engines: Pros and cons? In *Proceedings of the 20th Intersociety Energy Conversion Engineering Conference*, volume 2, pages 748–754, 1985.

[32] A. J. Ferrenberg and W. T. Webber. Regenerative internal combustion engine. United States Patent No. 4,790,284, 1988.

[33] A. J. Ferrenberg and W. T. Webber. Regenerative internal combustion engine. United States Patent No. 4,928,658, 1990.

[34] A. J. Ferrenberg. The single cylinder regenerated internal combustion engine. *SAE Technical Papers*, 1990, SAE 900911.

[35] A. J. Ferrenberg. Regeneration for reciprocating engines. In *Proceedings of the 26th Joint Propulsion Conference*, 1990, AIAA 90-2510.

[36] A. J. Ferrenberg. Low heat rejection regeneratred engines: A superior alternative to turbocompounding. *SAE Technical Papers*, 1994, SAE 940946.

[37] A. J. Ferrenberg and B. E. Williams. In-cylinder regenerated engines. *SAE Technical Papers*, 1995, SAE 950451.

[38] A. J. Ferrenberg. Regenerated engine with improved heating and cooling strokes. United States Patent No. 5,465,702, 1995.

[39] A. J. Ferrenberg. Regenerated engine with an improved heating stroke. United States Patent No. 5,632,255, 1997.

[40] F. Ruiz. A first look into the regenerative engine. *SAE Technical Papers*, 1989, SAE 890473.

[41] F. Ruiz. Regenerative internal combustion engine part I: Theory. *Journal of Propulsion and Power*, 6(2):203–208, 1990.

[42] F. Ruiz. Regenerative internal combustion engine part II: Practical configurations. *Journal of Propulsion and Power*, 6(2):209–213, 1990.

[43] S. Thyageswaran and F. Ruiz. Time-dependant analysis of the regenerative engine cycle. *SAE Technical Papers*, 1990, SAE 900912.

[44] J. M. Clarke. Ideal cycles incorporating heat exchange. *SAE Technical Papers*, 1990, SAE 900913.

[45] J. M. Clarke. High efficiency thermal regenerated internal combustion engine. United States Patent No. 5,540,191, 1996.

[46] J. M. Clarke and E. C. Fluga. Piston for a thermal regenerated engine. United States Patent No. 6,546,909, 2003.

[47] E. L. Warren. Two-stroke regenerative engine. United States Patent No. 6,116,222, 2000.

[48] A. Lowi and A. J. Ferrenberg. Stationary regenerator, regenerated, reciprocating engine. United States Patent No. 6,668,809, 2003.

[49] C. L. Cummins. *Internal Fire*. Carnot Press, 1989.

[50] R. B. Peterson. Thermocompression engine cycle with isothermal expansion. *Energy Sources*, 20:199–208, 1998.

[51] F. Ruiz. Thermodynamic modeling of the two-cylinder regenerative internal combustion engine. *SAE Technical Papers*, 1991, SAE 910346.

[52] F. M. White. *Fluid Mechanics*. McGraw Hill, fifth edition, 2003.

[53] M. McCaig and A. G. Clegg. *Permanent Magnets in Theory and Practice*. John Wiley and Sons, 1987.

[54] J. E. Gould. Permanent magnet applications. *IEEE Transactions on Magnetics*, 5(4):812–821, 1969.

[55] S. Defrancesco and V. Zanetti. Experiments on magnetic repulsion. *American Journal of Physics*, 51(11):1023–1025, 1983.

[56] A. Romer. Magnetic repulsion: An introductory experiment. *American Journal of Physics*, 41:1332–1336, 1973.

[57] R. S. Figliola and D. E. Beasley. *Theory and Design for Mechanical Measurements*. John Wiley and Sons, third edition, 2000.

Appendices

A Uncertainty Analysis for the Magnet Experiments

The Kline-McClintock method was used to estimate the uncertainty of the data for both the two-magnet experiment and the magnet-steel experiment [57]. The necessary component uncertainties are displayed in Table 5.1.

The two point calibrations were used to create linear functions that related the magnetic attraction force, F_M, and the load cell output voltage, V. Such a function is defined by

$$F_M = a + bV, \tag{A.1}$$

where

$$a = \frac{-F_C V_0}{V_C - V_0} \tag{A.2}$$

and

$$b = \frac{F_C}{V_C - V_0}. \tag{A.3}$$

The constants F_C and V_C are an average of the calibration force measurements and an average of the calibration voltage measurements, respectively, with the calibration mass hung from the load cell; V_0 is an average of the calibration voltage measurements with no load. By neglecting the precision error due to calibration, we can estimate the uncertainty for a by

$$u_a = \sqrt{\left(\frac{V_0 u_B}{V_C - V_0}\right)^2 + \left(\frac{F_C V_0 u_L}{(V_C - V_0)^2}\right)^2 + \left(\frac{F_C V_C u_L}{(V_C - V_0)^2}\right)^2}, \tag{A.4}$$

and the uncertainty for b by

$$u_b = \sqrt{\left(\frac{u_B}{V_C - V_0}\right)^2 + \left(\frac{F_C u_L}{(V_C - V_0)^2}\right)^2 + \left(\frac{F_C u_L}{(V_C - V_0)^2}\right)^2}. \tag{A.5}$$

The uncertainty for F_M, accounting only for bias error, can be estimated by

$$u_{Fm} = \sqrt{(V u_b)^2 + (b u_L)^2 + u_a^2}. \tag{A.6}$$

Precision error was considered using statistics from the data. The standard deviation, S_F, of the magnetic attraction force from the additional seven runs for one pair of magnets or for a magnet and a steel sample was used to account for variability of the data. The student-t statistic, $t_{6,90} = 1.943$, for six degrees of freedom and a confidence of 90 % was used as a multiplier to account for the precision error [57]. The overall uncertainty for F_M can be estimated by

$$U_{Fm} = \sqrt{u_{Fm}^2 + (t_{6,90} S_F)^2}. \tag{A.7}$$

B Program to Compute Magnet Constants

The following MATLAB program, which computes k_{Mag} and h_{Mag}, was used to characterize the D31 magnet.

```
function [h, k, res, devmin, devmax] = magcalc(force, dist, its)
```

`[h, k, res, resmin, resmax] = magcalc(force, dist, its)` computes the magnet pole offset, `h`, magnetic attraction force constant, `k`, residual vector, `res`, minimum deviation, `devmin`, and maximum deviation, `devmax`, given vectors of the magnetic attraction force, `force`, the separation distance, `dist`, and the number of iterations to be performed, `its`.

Iterations to find `k` *and* `h`

```
kit = []; hit = [];
kit(1) = 5e-006;        Guess for k, N·m^2
hit(1) = hgen(force, dist, kit(1));
for i = 2:its
    hit(i) = hgen(force, dist, kit(i-1));
    kit(i) = kgen(force, dist, hit(i));
end
h = hit(length(hit)); k = kit(length(kit));
res = norm(k./(h+dist).^2-force,2);
devmin = min(k./(h+dist).^2-force);
devmax = max(k./(h+dist).^2-force);
end
```

Program that iteratively finds `h`

```
function [h] = hgen(force, dist, kit)
hstep = 0:0.00001:0.003;        Guess range for h, m
n = length(hstep);
for i = 1:n
    ax = kit./(dist+hstep(i)).^2;
    r(i) = norm(ax-force,2)^2;
    clear ax
end
for  i = 1:n
    if r(i) == min(r)
        h = hstep(i);
    end
end
end
```

Program that computes `k`

```
function
[k] = kgen(force, dist, hit)
K = []; m = length(dist);
for i = 1:m
    K(i) = force(i).*(dist(i)+hit).^2;
end
k = mean(K);
end
```

C Half-Rhombic Drive Kinematic Equations

The kinematic equations for the half-rhombic drive were needed to design the miniature atmospheric engine simulator and to simulate the regenerator's dynamics. A schematic of the half-rhombic drive is shown in Fig. C.1, and its dimensions are listed in Table C.1.

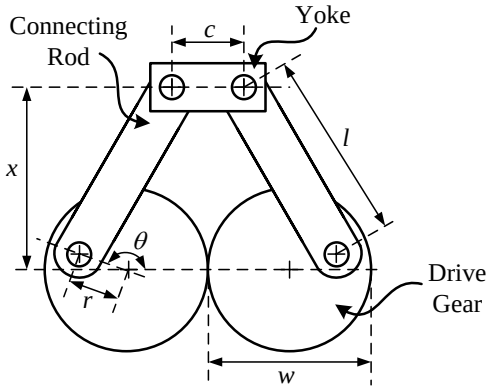

Figure C.1: A schematic of the half-rhombic drive.

Table C.1: Dimensions of the half-rhombic drive.

Dimension	Length, mm
c	15.2
l	19.1
r	4.5
w	25.4

The yoke is constrained to vertical motion only; and the position equation giving the height of the yoke from the centerline of the drive gears can be derived from the construction of a right triangle with the hypotenuse being the connecting rod. This position equation is written as

$$x = r\sin\theta + \left[l^2 - \left(\frac{w-c}{2}\right)^2 + (w-c)r\cos\theta - r^2\cos^2\theta\right]^{\frac{1}{2}}. \tag{C.1}$$

The height of the piston from bottom dead center, x_P, is found by subtracting the minimum height from Eq. (C.1), h_{Min}, for $0 \leq \theta \leq 2\pi$. This position equation is written as

$$x_P = x - h_{Min}. \tag{C.2}$$

The kinematic equations for velocity and acceleration are found with time derivatives. By taking the derivative of the position equation, Eq. (C.1), we can write the velocity equation as

$$\begin{aligned}\dot{x}_P =& r\dot{\theta}\cos\theta + \frac{1}{2}\left(2r^2\dot{\theta}\cos\theta\sin\theta - (w-c)r\dot{\theta}\sin\theta\right) \\ &\cdot\left[l^2 - \left(\frac{w-c}{2}\right)^2 + (w-c)r\cos\theta - r^2\cos^2\theta\right]^{-\frac{1}{2}}.\end{aligned} \tag{C.3}$$

And, by taking the derivative of the velocity equation, Eq. (C.3), we can write the acceleration equation as

$$
\begin{aligned}
\ddot{x}_P = & - r\dot{\theta}^2 \sin\theta + \overbrace{r\ddot{\theta}\cos\theta}^{\to 0} \\
& - \frac{1}{4}\Big(2r^2\dot{\theta}\cos\theta\sin\theta - (w-c)r\dot{\theta}\sin\theta\Big) \\
& \cdot \left[l^2 - \left(\frac{w-c}{2}\right)^2 + (w-c)r\cos\theta - r^2\cos^2\theta\right]^{-\frac{3}{2}} \\
& + \frac{1}{2}\Bigg(- 2r^2\dot{\theta}^2\sin^2\theta + 2r^2\dot{\theta}^2\cos^2\theta + \overbrace{2r^2\ddot{\theta}\cos\theta\sin\theta}^{\to 0} \\
& - (w-c)r\dot{\theta}^2\cos\theta - \overbrace{(w-c)r\ddot{\theta}\sin\theta}^{\to 0}\Bigg) \\
& \cdot \left[l^2 - \left(\frac{w-c}{2}\right)^2 + (w-c)r\cos\theta - r^2\cos^2\theta\right]^{-\frac{1}{2}}.
\end{aligned}
\tag{C.4}
$$

For the dynamic simulations, the input shaft speed was assumed to be constant. Thus, as indicated in Eq. (C.4), all terms with $\ddot{\theta}$ as a factor are zero.

D Programs to Simulate the Regenerator's Dynamics

The dynamic model was written in MATLAB, and a fourth-order Runge-Kutta algorithm was used to solve the differential equations. When an event flagged the algorithm, the simulation was paused; a logic structure then determined the next phase. The following program, `regendynmod.m`, is the main program for the dynamic model.

```
function [] = regendynmod()
```

This program simulates the regenerator's dynamics given the dimensions of the half-rhombic mechanism, the dimensions of the regenerator, magnet constants, and other physical constants.

```
clear all
close all
global mc
```

User input

Simulation parameters

```
cycles = 1;          Number of cycles to be simulated
res = 1000;          Plot resolution
mc.rpm = 1000;       Mechanism input speed, rpm
```

Spring parameters

```
k = 1.90;          Spring stiffness, lb/in
free = 0.625;      Spring free length, in
comp = 0.096;      Spring solid length, in
precomp = 0.3;     Spring rest compression
```

Half-rhombic mechanism dimensions

```
r = 0.176;         Crank radius, in
l = 0.75;          Connecting rod length, in
w = 1;           Gear pitch diameter, in
c = 0.6;         Yoke width, in
htrav = 0.538;     Linkage minimum travel height, in
```

Regenerator parameters

```
tdc = 0.366;       Top dead center, in
H = 0.188;       Height of the regenerator, in
mc.rtrav = 0.25;       Regenerator travel, TDC
clr = 0.01;        Regenerator to TDC clearance, in
cap = 0.480;       Cap thickness, in
m = 1.81;        Mass of regenerator, g
d = 0.366;       Cylinder inner diameter, in
h = 0.008;       Regenerator to cylinder radial clearance, in
mc.n = 12;       Number of regenerator ports
p = 0.047;       Regenerator port diameter, in
```

Fluid properties

```
mc.mu = 184.6e-7;        Viscosity, N·s/m^2
mc.rho = 1.2;        Density, kg/m^3
```

Magnet constants

```
mc.kmag = 0.483455*6.52e-6;        Magnetic attraction force constant, N·m^2
mc.hmag = 1.14e-3;         Magnet pole offset, m
```

Unit conversions

```
in_m=25.4e-3;
lbpin_npm=4.448/25.4e-3;
g_kg=1e-3;
mc.m=m*g_kg;
mc.k=k*lbpin_npm;
mc.free=free*in_m;
mc.comp=comp*in_m;
mc.r=r*in_m;
mc.l=l*in_m;
mc.w=w*in_m;
mc.c=c*in_m;
mc.htrav=htrav*in_m;
mc.tdc=tdc*in_m;
mc.H=H*in_m;
mc.clr=clr*in_m;
mc.cap=cap*in_m;
mc.d=d*in_m;
mc.h=h*in_m;
mc.p=p*in_m;
```

Calculated parameters

```
mc.lspring = (1-precomp)*mc.free;
mc.hface = mc.lspring+mc.H+mc.cap;
mc.htop = mc.H+mc.clr+mc.tdc+mc.cap;
mc.hstop = (1-mc.rtrav)*mc.tdc+mc.hface;
mc.alpha = mc.d^2/(mc.n*mc.p^2+4*(mc.h*mc.d-mc.h^2));
mc.A_a = pi/4*((mc.d-2*mc.h)^2-mc.n*mc.p^2);
C_g = 4*pi*mc.mu*mc.alpha*mc.H*(mc.d-2*mc.h)/mc.h;
C_p = 8*mc.mu*mc.alpha*mc.n*pi*mc.H;
mc.C_tot = C_g+C_p;
mc.g = 9.807;
```

Simulation of the regenerator's dynamics

Define the ODE solver options

```
func = {@topdwell @interaction @coupled @bottomdwell};
options = {odeset('event',@event1) odeset('event',@event2) ...
    odeset('event',@event3) odeset('event',@event4)};
```

Initialize the ODE solver

```
tf = cycles*(mc.rpm/60)^-1;
step = tf/res; t0 = 0;
xr0 = [mc.tdc+mc.clr 0]; phase = 1;
T = t0; t = t0;
XR = xr0;
tspan = [t tf];
phaview = []; phaview(1) = 1;
eveview = []; tview = []; simcheck = [];
```

The main loop

```
while t<tf
    [TRI XRI TE XE IE] = ode45(func{phase},tspan,xr0,options{phase});
    T = [T; TRI(2:length(TRI))];
    XR = [XR; XRI(2:length(TRI), :)];
    t = T(length(T));
    xr0 = XRI(length(TRI),:);
    tspan = [t tf];
```

```
    switch phase
        case 1
            if length(IE) == 1;
                phase = 2;
            end
        case 2
            if length(IE) == 1;
                switch IE
                    case 1
                        phase = 1;
                        xr0(2) = 0;
                    case 2
                        phase = 4;
                        xr0(2) = 0;
                    case 3
                        phase = 3;
                        xp = xpiston(t);
                        xr0(2) = xp(2);
                end
            end
        case 3
            if length(IE) ==  1;
                if IE == 1
                    phase = 2;
                else
                    phase = 4;
                    xr0(2) = 0;
                end
            end
        case 4
            if length(IE) == 1;
                if IE == 1
                    phase = 2;
                else
                    phase = 3;
                    xp = xpiston(t);
                    xr0(2) = xp(2);
                end
            end
    end
    eveview = [eveview IE];
    tview = [tview TE];
    simcheck = [simcheck XR(length(XR),1)];
    phaview = [phaview phase];
end
```

Check the spring length

```
if mc.lspring >= mc.free
    error('Spree free length is too small!')
elseif mc.hstop-mc.htop < 1.1*mc.comp
    error('Spring compressed length is too large!')
end
```

Check the Reynolds numbers

```
regpist=xpiston(T);
maxvel=max(XR(:,2)-regpist(:,2));
RPort=(mc.rho*mc.alpha*maxvel*mc.p)/mc.mu
RGap=(mc.rho*mc.alpha*maxvel*2*mc.h)/mc.mu
```

Simulation output

```
z = t0:step:tf; y = xpiston(z);
figure(1)
plot(z,y(:,1)*1000,'b','LineWidth',2)
hold on
plot(T,XR(:,1)*1000,'k','LineWidth',2)
plot(tview, simcheck(1:length(simcheck)-1)*1000, 'o','MarkerSize',...
5,'MarkerFaceColor','b','MarkerEdgeColor','k', 'LineWidth', 2)
hold off
axis([t0 tf -1 11])
h=gca;
grid on
set(h,'XMinorTick','on','YMinorTick','on')
set(h,'GridLineStyle', '-.')

tview
simcheck
eveview
phaview
dt=tview(end)-tview(3)

end
```

Functions for each phase of motion

The numbers of both the phases and events correspond to the numbers of the main-loop logic structure above.

1: Top Dwell

```
function [dxr] = topdwell(t,xr)
dxr(1,1) = 0;
dxr(2,1) = 0;
end
```

2: Interaction

```
function [dxr] = interaction(t,xr)
global mc
[Fs Fm Fv Fp] = forcemake(t, xr');
dxr(1,1) = xr(2);
dxr(2,1) = (Fs+Fp-Fv-Fm-mc.m*mc.g)/mc.m;
end
```

3: Coupled

```
function [dxr] = coupled(t, xr)
xp = xpiston(t);
dxr(1,1) = xp(2);
dxr(2,1) = xp(3);
end
```

4: Bottom dwell

```
function [dxr] = bottomdwell(t, xr)
dxr(1,1) = 0;
dxr(2,1) = 0;
end
```

Functions for ODE solver events

Top dwell

```
function [value, isterminal, direction] = event1(t,xr)
global mc
[Fs Fm Fv Fp] = forcemake(t, xr');
value = Fs+Fp-Fm-Fv-mc.m*mc.g;        1: To interaction
isterminal = 1;
direction = -1;
end
```

Interaction

```
function [value, isterminal, direction] = event2(t,xr)
global mc
xp = xpiston(t);
value(1) = xr(1)-mc.tdc-mc.clr;        1: To top dwell
value(2) = xr(1)+mc.hface-mc.hstop;        2: To bottom dwell
value(3) = xr(1)-xp(1);        3: To coupled
isterminal = [1 1 1];
direction = [1 -1 -1];
end
```

Coupled

```
function [value, isterminal, direction] = event3(t,xr)
global mc
xp = xpiston(t);
[Fs Fm Fv Fp] = forcemake(t, xr');
value(1) = Fs-Fm-Fv-mc.m*mc.g-mc.m*xp(3);        1: To interaction
value(2) = xr(1)+mc.hface-mc.hstop;        2: To bottom dwell
isterminal = [1 1];
direction = [1 -1];
end
```

Bottom dwell

```
function [value, isterminal, direction] = event4(t,xr)
global mc
xp = xpiston(t);
[Fs Fm Fv Fp] = forcemake(t, xr');
value(1) = -Fs-Fp+Fm+Fv+mc.m*mc.g;        1: To interaction
value(2) = xp(1)+mc.hface-mc.hstop;        2: To coupled
isterminal = [1 1];
direction = [-1 1];
end
```

Force computation

```
function [Fs Fm Fv Fp] = forcemake(t, xr)
xp = xpiston(t);
Fs = springforce(xr);
Fm = magforce(xr, xp);
Fv = dampforce(xr, xp);
Fp = pressforce(xr, xp);
end
```

The main program, `regendynmod.m`, requires several subprograms. They were written separately so that modifications can be easily made. All of the remaining programs in this chapter are subprograms for `regendynmod.m`.

The following subprogram computes the kinematic quantities of the piston. It could be rewritten for any conceivable drive mechanism by deriving new kinematic equations and rewriting the program appropriately.

```
function [xp] = xpiston(t)
```

`[xp] = xpiston(t)` computes the vector of the kinetics of the piston, `xp`, given the time, `t`.

```
global mc
thetad = mc.rpm*2*pi/60;
theta = thetad.*t;
```

Position

```
xp(:,1) = mc.r*sin(theta)+...
    (mc.l^2-((mc.w-mc.c)/2)^2+(mc.w-mc.c)*mc.r*cos(theta)...
    -mc.r^2*(cos(theta)).^2).^(1/2)-mc.htrav;
```

Velocity

```
xp(:,2) = mc.r*cos(theta)*thetad+(1/2)*(mc.l^2-((mc.w-mc.c)/2)^2+...
    (mc.w-mc.c)*mc.r*cos(theta)-mc.r^2*(cos(theta)).^2).^(-1/2).*...
    (2*mc.r^2*cos(theta).*sin(theta)*thetad-(mc.w-mc.c)*...
    mc.r*sin(theta)*thetad);
```

Acceleration

```
xp(:,3) = -mc.r*sin(theta)*thetad^2-(1/4)*(mc.l^2-((mc.w-mc.c)/2)^2+...
    (mc.w-mc.c)*mc.r*cos(theta)-mc.r^2*(cos(theta)).^2).^(-3/2).*...
    (2*mc.r^2*cos(theta).*sin(theta)*thetad-(mc.w-mc.c)*mc.r*sin(theta)...
    *thetad).^2+(1/2)*(mc.l^2-((mc.w-mc.c)/2)^2+(mc.w-mc.c)*...
    mc.r*cos(theta)-mc.r^2*(cos(theta)).^2).^(-1/2).*...
    (2*mc.r^2*thetad^2*((cos(theta)).^2-(sin(theta)).^2)-(mc.w-mc.c)*...
    mc.r*cos(theta)*thetad^2);
end
```

The following subprogram computes the drag force on the regenerator.

```
function [Fv] = dampforce(xr, xp)
```

`[Fv] = dampforce(xr, xp)` computes the drag force for the regenerator, `Fv`, given the vector of the kinetics of the regenerator, `xr`, and the vector of the kinetics of the piston, `xp`.

```
global mc
Fv = -mc.C_tot*(xp(:,2)-xr(:,2));
end
```

The following subprogram computes the magnetic attraction force on the regenerator.

```
function [Fm] = magforce(xr, xp)
```

`[Fm] = magforce(xr, xp)` computes the magnetic attraction force, `Fm`, given the vector of the kinetics of the regenerator, `xr`, and the vector of the kinetics of the piston, `xp`.

```
global mc
x = xr(:,1)-xp(:,1);
Fm = mc.kmag./(x+mc.hmag).^2;
end
```

The following subprogram computes the force due to the pressure difference across the regenerator.

```
function [Fp] = pressforce(xr, xp)
```

`[Fp] = pressforce(xr, xp)` computes the force due the pressure difference across the regenerator, `Fp`, given the vector of the kinetics of the regenerator, `xr`, and the vector of the kinetics of the piston, `xp`.

```
global mc
P_diff = 32*mc.mu*mc.alpha*(xp(:,2)-xr(:,2))*mc.H/mc.p^2;
Fp = P_diff*mc.A_a;
end
```

The following subprogram computes the spring force on the regenerator.

```
function [Fs] = springforce(xr)
```

`[Fs] = springforce(xr)` computes the spring force, `Fs`, given the vector of the kinetics of the regenerator, `xr`.

```
global mc
lc = mc.free-(mc.tdc+mc.hface+mc.clr-mc.htop);
Fs = mc.k*(lc+mc.tdc+mc.clr-xr(:,1));
end
```

E Program for Regenerator Experiments

The following MATLAB program was used for the autonomously-reciprocating-regenerator experiments; it compared the data to the piston's kinematics and computed a vector comprised of times corresponding to the data.

```
function [t]=datamatch(piston,regen,tf)
```

`[t]=datamatch(piston,regen,tf)` computes the vector of times, `t`, given the vectors of experimental data, `piston` and `regen`, and the final time, `tf`. The vector `t` can be used to link the experimental data to the simulation of the regenerator's motion.

```
thresh=8;
tol=0.01;
tcheck=0:0.00001:tf;
test=0;
for i=1:length(piston)
    for j=1:length(tcheck)
        pis=xpiston(tcheck(j));
        diff=abs(pis(1)*1000-piston(i));
        if diff<tol
            if piston(i)==regen(i) & piston(i)>thresh
                t(i)=tcheck(j);
                test=1;
                break
            end
            if sign(pis(2))==-1
                t(i)=tcheck(j);
                test=1;
                break
            end
            if regen(i)>thresh & regen(i)~=piston(i)
                t(i)=tcheck(j);
                test=1;
                break
            end
        end
    end
    if test==0
        i
        error('tolerance not met')
    end
    test=0;
end
end
```

F Uncertainty Analysis for the Pressure Experiments

The Kline-McClintock method was used to estimate the uncertainty for the pressure experiments [57]. The necessary component uncertainties are displayed in Table 8.1.

The two-point calibrations were used to create linear functions that related pressure, P, and pressure transducer output voltage, V. Such a function is defined by

$$P = a + bV, \tag{F.1}$$

where

$$a = \frac{P_{Atm}V_C - P_C V_{Atm}}{V_C - V_{Atm}} \tag{F.2}$$

and

$$b = \frac{P_C - P_{Atm}}{V_C - V_{Atm}}. \tag{F.3}$$

The constants P_C and P_{Atm} are the measurements for calibration pressure and atmospheric pressure, respectively; V_C and V_{Atm} are the corresponding pressure transducer output voltages. If the precision error due to calibration is neglected, the uncertainty for a can be estimated by

$$u_a = \left[\left(\frac{V_C u_{PAtm}}{V_C - V_{Atm}} \right)^2 + \left(\frac{V_{Atm} u_{PC}}{V_C - V_{Atm}} \right)^2 + \left(\frac{(P_C V_{Atm} - P_{Atm} V_{Atm}) u_{PT}}{(V_C - V_{Atm})^2} \right)^2 + \left(\frac{(P_{Atm} V_C - P_C V_C) u_{PT}}{(V_C - V_{Atm})^2} \right)^2 \right]^{\frac{1}{2}}, \tag{F.4}$$

and the uncertainty for b can be estimated by

$$u_b = \left[\left(\frac{u_{PC}}{V_C - V_{Atm}} \right)^2 + \left(\frac{u_{PAtm}}{V_C - V_{Atm}} \right)^2 + \left(\frac{(P_{Atm} - P_C)u_{PT}}{(V_C - V_{Atm})^2} \right)^2 + \left(\frac{(P_C - P_{Atm})u_{PT}}{(V_C - V_{Atm})^2} \right)^2 \right]^{\frac{1}{2}}. \quad \text{(F.5)}$$

The pressure ratio with respect to minimum cycle pressure can be written as

$$P_R = \frac{P_{Max}}{P_{Min}}, \quad \text{(F.6)}$$

where P_{Max} is the maximum cycle pressure and P_{Min} is the minimum cycle pressure. The uncertainty of the pressure measurement, which accounts only for bias error, can be written as

$$u_P = \sqrt{(V u_b)^2 + (a u_{PT})^2 + u_a^2}. \quad \text{(F.7)}$$

The overall uncertainty for P_R, which neglects precision error, can now be written as

$$U_{PR} = \sqrt{\left(\frac{u_{PMax}}{P_{min}} \right)^2 + \left(\frac{P_{Max} u_{PMin}}{P_{Min}^2} \right)^2}. \quad \text{(F.8)}$$

The pressure ratio with respect to atmospheric pressure, P_{Atm}, can be written as

$$P_{RAtm} = \frac{P_{Max}}{P_{Atm}}. \quad \text{(F.9)}$$

Like the uncertainty for P_R, the overall uncertainty for P_{RAtm} can be estimated by

$$U_{PRAtm} = \sqrt{\left(\frac{u_{PMax}}{P_{Atm}} \right)^2 + \left(\frac{P_{Max} u_{PAtm}}{P_{Atm}^2} \right)^2}. \quad \text{(F.10)}$$

For the long-duration pressure experiments, precision error was considered using statistics from the data. The standard deviation of the pressure measurements, S_P, was used to account for variability of the data. The student-t statistic for six degrees of freedom and a confidence of 90 %, $t_{6,90} = 1.943$, was used as a multiplier to account for the precision error [57]. The overall uncertainty for P can be estimated by

$$U_P = \sqrt{u_P^2 + (t_{6,90} S_P)^2}. \tag{F.11}$$